3-10-2008

Radial velocities of stars in the Galactic Center

Qingfeng Zhu

Rolf Kudritzki

Donald Figer

Radial Velocities of Stars in the Galactic Center [1]

QINGFENG ZHU[2], ROLF P. KUDRITZKI[3], DONALD F. FIGER[2], FRANCISCO NAJARRO[4] and DAVID MERRITT[5]

ABSTRACT

We present results from K band slit scan observations of a $\sim20''\times20''$ region of the Galactic center (GC) in two separate epochs more than five years apart. The high resolution (R = $\frac{\lambda}{\Delta\lambda}\geq$14,000) observations allow the most accurate radial velocity and acceleration measurements of the stars in the central parsec of the Galaxy. Detected stars can be divided into three groups based on the CO absorption band heads at $\sim$2.2935 μm and the He I lines at $\sim$2.0581 μm and $\sim$2.112, 2.113 μm: cool, narrow-line hot and broad-line hot. The radial velocities of the cool, late-type stars have approximately a symmetrical distribution with its center at $\sim$-7.8$\pm$10.3 km s^{-1} and a standard deviation $\sim$113.7$\pm$10.3 km s^{-1}. Although our statistics are dominated by the brightest stars, we estimate a central black hole mass of 3.9$\pm$1.1$\times10^6$M$_\odot$, consistent with current estimates from complete orbits of individual stars. Our surface density profile and the velocity dispersion of the late type stars support the existence of a low density region at the Galactic center suggested by earlier observations. Many hot, early-type stars show radial velocity changes higher than maximum values allowed by pure circular orbital motions around a central massive object, suggesting that the motions of these stars greatly deviate from circular orbital motions around the Galactic center. The correlation between the radial velocities of the early type He I stars

[2]Chester F. Carlson Center for Imaging Science, Rochester Institute of Technology, 54 Lomb Memorial Drive, Rochester, NY 14623-5604; zhuqf@cis.rit.edu; figer@cis.rit.edu

[3]Institute for Astronomy, University of Hawaii, 2680 Woodlawn Drive, Honolulu, HI 96822; kud@ifa.hawaii.edu

[4]Insituto de Estructura de la Materia, Consejo Superior de Investigaciones Científicas, Calle Serrano 121, 28006, Madrid, Spain; najarro@damir.iem.csic.es

[5]Department of Physics and Center for Computational Relativity and Gravitation, 85 Lomb Memorial Drive, Rochester, NY 14623-5604; merritt@astro.rit.edu

and their declination offsets from Sagittarius A* suggests that a systematic rotation is present for the early-type population. No figure rotation around the Galactic center for the late type stars is supported by the new observations.

Subject headings: Galaxy: center, Stars: kinematics, Techniques: spectroscopic

1. Introduction

The central half parsec in the Galactic center (GC) contains $\sim 4 \times 10^6$ M$_\odot$ of mass which dominates the gravitational potential within several parsecs from the GC. This fact raises many questions concerning the composition and origin of the central mass and its effects on stellar objects in its vicinity. Evidence strongly supports that a super massive black hole (SMBH) is present at the GC (Ghez et al. 2000; Schödel et al. 2002). One of the most important tasks is to determine the mass of the central object, or equivalently, to measure the gravitational potential of the central object. The gravitational potential can be probed by measuring bulk motions of the ionized gas in the region (Lacy et al. 1982; Serabyn & Lacy 1985) or by tracing a single star's 3D motion around the central mass (Schödel et al. 2002; Ghez et al. 2005). These methods give similar estimates of the central black mass, with $M \simeq 3 \times 10^6$ $M_\odot$, although a Sun-GC distance of 10 kpc was used in some of the earlier works (Lacy et al. 1982; Serabyn & Lacy 1985), which could result in an overestimate of the enclosed mass. Both Schödel et al. (2002) and Ghez et al. (2005) used a value of 8 kpc, which is also the value we assumed in the current work.

We can also estimate the central mass by using statistical mass estimators, which are based on the phase space distributions of particles in dynamical systems. These mass estimators provide a cross-check for other methods. We should note that not every star is suitable for the statistical method. Many mass estimators ask for a certain degree of velocity anisotropy for the dynamical system under study. One such widely-used mass estimator, derived by Bahcall & Tremaine (1981) (BT mass estimator), assumes that the velocities of stars in the system are isotropic, which means that the stars have lived long enough so that their motions are relaxed through close encounters. Two-body relaxation time is related to the mean stellar mass, the velocity dispersion and the stellar density (Binney & Tremaine 1987) and has a value $\sim 6 \times 10^9$ yrs at the distance of ~ 0.7 pc from a black hole with a mass of 3.7×10^6M$_\odot$ for a spherical velocity ellipsoid (Merritt & Szell 2006). Certainly, not all stars in the GC have lived such a long time. Studies show that the central parsec of the GC is populated by several stellar components, including low mass red giants, hot He I emission line stars, some luminous M-supergiant and asymptotic giant branch (AGB) stars, and embedded near-IR featureless stars (Allen et al. 1990; Krabbe et al. 1991; Tamblyn et al.

1996; Genzel et al. 1996; Blum et al. 1996b; Najarro et al. 1997; Genzel et al. 2000, 2003). Among these stars, only low mass red giant branch stars have lifetimes long enough so that the two-body relaxation can be effective (Davidge et al. 1997). Previous studies suggest that the velocities of late type stars in the inner parsec of the GC are close to being isotropic (Genzel et al. 1996, 2000). Thus it is possible to use mass estimators derived for isotropic velocity distributions to estimate the central black mass, but it is also important to try other estimators, like ones based on the Virial Theorem, which are valid for any degree of anisotropy.

The GC is generally believed to be hostile to spontaneous star formation through fragmentation and contraction of molecular clouds. Extreme physical conditions, such as strong gravitational tidal forces of the central object, large turbulent velocities inside molecular clouds and strong magnetic fields can prevent star formation in the region (Morris 1993). However, discoveries of young populations such as M supergiants, AGB stars, hot emission line stars and main sequence stars (Genzel et al. 2003; Ghez et al. 2005) pose a great challenge to the star formation theory in the GC. Several scenarios have been proposed to explain the observed young stellar populations in the GC. These scenarios include the in situ star formation following the cloud collapse triggered by compressing shocks due to cloud-cloud collisions (Morris 1993) and the insertion of young stars into the inner parsec of the Galaxy through mass segregation after the stars formed elsewhere (Gerhard 2001; Portegies Zwart et al. 2003). Additionally, observations suggest two types of hot emission line stars are present in the inner parsec of the Galaxy (Paumard et al. 2001; Tanner et al. 2006). One type of stars show narrow absorption doublet in the 2.112/2.113 μm He I lines and narrow emission in the 2.058 μm He I line. The other type shows broad emission in these He I lines. These two types may represent two different evolutionary stages of massive stars (Paumard et al. 2001, 2003).

We carried out a set of high resolution spectroscopic survey observations of the stars in the GC in order to acquire accurate radial velocity measurements of the stars of both late (cool) and early (hot) types in two different epochs separated by $\sim$5.8 years. The new observations allow us to estimate the mass of the central black hole using the stellar velocity distribution and study the velocity changes of these stars between the two epochs and other properties of the stars in the region.

In § **2**, we introduce our observational method and data reduction procedure. We present the results of the data analysis in § **3**. We discuss the implications of the results in section § **4** and summarize our findings in § **5**.

2. Observations and Data Reduction

2.1. Observations

Four slit scan observations were conducted over a $\sim 20'' \times 20''$ region in the GC with the near-infrared spectrometer (NIRSPEC) on the Keck II telescope during June 4th 1999, July 4th 1999, April 13th 2005 and April 14th 2005. We refer to these observations as "GC1", "GC2", "GC3" and "GC4" later in this paper. The sky area covered by each scan is indicated in Figure 2. The corresponding observational parameters are listed in Table 1. The high resolution cross-dispersing mode of the instrument was used to acquire spectra in the range of 2.04 to 2.38 μm to include the ^{12}CO (2-1) first overtone band head features at $\sim$2.2935 μm and the Earth's atmospheric features between 2.04 and 2.06 μm. Spatial-spectral images of multiple echelle orders were obtained with the 1024×1024 pixel InSb detector. The NIRSPEC-6 and NIRSPEC-7 filters were used during the slit scans. The spectral ranges of echelle orders covered by each scan can be found in Table 2. During each scan, the telescope was stepped left to right across the field of the observations and an image rotator controlled a long slit to keep slit orientation along the north-south direction. Slit viewing camera (SCAM) images were taken simultaneously with spectra. These images are used to determine the location and orientation of the slit when the spectra were acquired. The width of the slit was chosen to match seeing at the time when the observations were carried out. The FWHM of seeing estimated using SCAM images is 0.6″, 0.4″, 0.5″, and 0.5″ for data obtained in GC1, GC2, GC3, and GC4, respectively. The estimated resolving power (R= $\frac{\lambda}{\Delta\lambda}$) was $\sim$ 14,000 during GC1, $\sim$ 23,300 during GC2 and $\sim$ 16,700 during GC3 and GC4. Here, $\Delta\lambda$ is the width (FWHM) of arc lamp lines in our calibration frames and is measured at λ=2.1714 μm. Necessary flat, sky (dark spot) and wavelength calibration frames were also acquired with the same instrument setting for each night.

2.2. Data Reduction

To compare results from different epochs, it is necessary to reduce data in a consistent way to avoid artifacts associated with different methods. We developed an IDL data reduction code, which is applied to all data sets. We removed background emission by subtracting an average dark spot image from target images. However, this procedure does not correct for sky variation during the scans, which we have to tolerate. Additional contamination may come from data which were taken before our observations. Unexpected lines or stripes resulting from bright sources in the earlier observations are seen in some of our images as ghost features. Fortunately, we have those data, so we can determine the contaminating

sources by carefully examining our slit scan images and data taken immediately before our observations. We subtract an optimal fraction of each contaminating frame from our target images so that the resulting images contain minimum amount of unwanted features (the correlation coefficient between our data and the contaminating frame reaches minimum for the region where the unwanted features were spotted). This method removes most ghost features, such as the contamination caused by bright arc lamp lines. After the subtractions, we divide the resulting frames by the QTH lamp images (flat) to correct for detector response variation. Finally, the data are treated with the bad pixel cleaning procedure described in Figer et al. (2003).

Three images of a bright star, Quintuplet star #3 (Q3), taken with the same instrument setting, are used as our telluric standard for each night. The telescope was offset when these images were taken so that Q3 is present at different locations along the slit in each image. We subtract three images from each other to remove background emission. Two resulting images with positive and negative stars are flat-fielded and treated with the bad pixel cleaning procedure. The arc, etalon lamp wavelength calibration frames are also flat-fielded and cleaned of bad pixels. These frames are used in rectification procedure to get accurate wavelength scale and de-wrapped orders for target images.

To obtain an accurate wavelength scale, we use the follow procedure to reduce observational data. First, we use Arc lamp lines (including Ar, Ne, Kr and Xe lines) with known wavelengths to set the wavelength scale across the etalon frame. The etalon line wavelengths are measured based on this wavelength scale. The etalon equation ($\lambda = \frac{2t}{N}$) is solved to find the etalon plate thickness (t) and the orders (N) of the etalon lines. Theoretical etalon line wavelengths are calculated using the derived etalon thickness and order numbers. Finally, the new etalon line wavelengths are used to derive de-wrapping matrices and calibration reference wavelengths for the target images. Ideally, one etalon thickness should be valid for all etalon orders present in the same instrument setting. However, this is generally not the case. To achieve the best wavelength calibration, we use different etalon thicknesses for echelle orders. For echelle orders with at least two Arc lamp lines bracketing a big portion of the orders, e.g. orders #32 and #34-36, this method gives wavelengths with calibration errors $\sim$3 km s^{-1}. For the echelle order #37, this method gives bigger errors, around 7 km s^{-1}. In the order #33, which contains the CO band head features, there are only two known Arc lamp lines which are close to each other in the order. Using these two lines to calibrate wavelengths will result in huge wavelength errors for pixels far from these Arc lamp lines. In this case, we carefully choose the etalon thickness so that wavelength uncertainties of rectified Arc lamp lines in neighboring orders vary monotonically. After doing this, two Arc lines have wavelength errors $\sim$3 km s^{-1}. These errors are estimated by measuring the line wavelengths in the rectified Arc lamp line frames using the de-wrapping matrices derived

from the etalon wavelengths.

After rectification, target frames are divided into individual orders. Stars are present as bright strips along the wavelength direction in the rectified orders. An example of rectified orders is shown in Figure 3 (bottom panel). Two prominent spectral features in the image are vertical telluric (CO_2) absorption lines and bright 2.058 μm He I line emission from local ionized gas in the GC. Spectra of individual stars are extracted from each order with an extraction window of 5 pixels. Local sky background at each wavelength is estimated from values of pixels (1 pixel wide window) immediately above and below the pixels belonging to stars and subtracted from the stellar spectra. We sacrifice some s/n to avoid bad background extraction in the crowded field. Spectrum of the telluric standard star is extracted in the same way. Finally, the target spectra are divided by the spectrum of the standard star to correct for absorption by the Earth's atmosphere.

In rectified orders, stellar spectra are usually shifted along the dispersion direction because stars are generally not centered in the slit (Figure 3). We can find the amount of shift by cross-correlating the telluric features in stellar spectra with those in the spectrum of the brightest object in our data sets (usually IRS7). The cross-correlation produces the distribution of the offset within the slit for four data sets (Figure 4). Because the location of a star in the slit is random, it is not surprising that the offset has a normal distribution. Gaussian fits of the distributions are also shown in the figure and the width of the corresponding Gaussian fit is indicated in each plot. These widths are consistent with the sizes of slits used in four slit scans, which again proves that our assumption of a normal distribution is correct. We can see from the figure that centers of the distributions are usually offset from zero, indicating that IRS7 is normally not centered in our slits. The actual shift to which each extracted spectrum is subjected is the difference between the calculated shift and the center of the normal distribution. Finally, the correct shift is applied to each spectrum.

Some observational parameters, such as telescope pointing and slit orientation at the time when data were taken are stored in headers of raw data files. However, the stored values are not accurate, especially when the telescope tracking and/or image rotator control fails, which happened during the observations of July, 1999. Thus, instead of using the stored parameters, we use the sky images taken by SCAM during the scan observations to calculate offsets of telescope pointing and position angles of the slit by matching positions of two bight stars (IRS11NE and IRS28) in the field. Coordinates of the two stars are taken from Figer et al. (2003). This method allows better estimations of telescope pointing and slit orientation. These parameters, together with offsets of stars from the edge of the rectified orders, are used to calculate coordinates of stars.

Depending on the width and tilting angle of the slit and the size of telescope steps, the

same star may be present in several slit positions (different files). Spectra of same stars need to be coadded before we make further analysis to avoid miscount of stars and to improve s/n. We use stellar positions as the primary criterion to identify different stars. At the same night, all candidate stars with coordinate offsets less than 1.5″ are probably the same star. However, if we extract more than one spectrum from the same file, the spectra are considered from different stars no matter how close the stars are in space. To discriminate stars that are too close in coordinates, stellar spectra are also used as the additional criterion. Spectra of the same star are assumed to have similar line profiles and Doppler shifts during the same night. The coadded spectra are then used to find radial velocities for cool and hot stars based on different spectral features. Spectra showing 2.2935 μm CO band head absorption features are considered from relatively cool giant or super giant stars. Absorption features at $\sim$2.112 and 2.113 μm and emission feature at $\sim$2.058 μm help us to identify two types of hot stars (narrow-line and broad-line He I stars) described in Tanner et al. (2006) and Paumard et al. (2001). The positions of all stars of three types found in this work are shown in Figure 5.

3. Results

K band slit scan observations of the central parsec of the Galaxy are carried out in two different epochs. Results from the first epoch have been presented by Figer et al. (2003) for cool stars and by Tanner et al. (2006) for hot stars. In the current work, we combine the data from the two epochs to study the spatial distributions and the accelerations of early and late populations in the inner parsec of the Galaxy. By using an improved data reduction procedure, we have identified 123 cool stars and 29 hot stars. We provide the most accurate radial velocity measurements of these stars at two epochs. Among the detected hot stars, 20 stars fall into the narrow-line category and 9 stars fall into the broad-line category. In the following, we present results from our analysis.

3.1. Cool Stars

The distinct ^{12}CO (2-1) band head features with a sharp edge at 2.2935 μm are used to find radial velocities of cool stars. The spectrum of Arcturus (Ramirez et al. 1997) is used as the template. We cross-correlate the coadded stellar spectra with the template spectrum to find the best shifts and correlation coefficients. A big coefficient ($\geq$0.6) indicates that the stellar spectrum under examination shows evident CO band head features and that the star is late-type. The criterion is picked based on visual inspection of the results of cross-

correlation. To understand the meaning of the criterion, we simulate measured spectra by adding a certain amount of white noise to the template spectrum. Our simulation shows that the cross-correlation coefficient drops below 0.6 when s/n is smaller than 1.7. The median value of s/n for these spectra is $\sim$4.4. Stellar radial velocities are computed from wavelength shifts of the CO band heads. We compute spectral types of these stars using a linear relationship between the equivalent width of the CO band heads and the surface temperature of a cool star (Figer et al. 2003). The derived spectral type is used to make an additional correction for the wavelength shift due to the stellar surface temperature. This correction is typically less than 4 km s^{-1} (Figer et al. 2003). The wavelength shift caused by the Earth's motion relative to the Sun is taken into account. The values are computed using the macro, bary.pro, from the IDL Astronomy User's Library. This correction is computed as +6.6, -8.1, 26.3, and 26.0 km s^{-1} for four data sets, respectively. Here a positive velocity indicates a motion toward the GC.

The total numbers of cool stars identified in the four slit scans are 98, 30, 68, and 68, respectively. In order to compare the stellar velocities in the two epochs more than five years apart, we combine two data sets in the year of 1999 (GC1 and GC2) and two data sets in the year of 2005 (GC3 and GC4). A total of 102 cool stars are included in the combined 1999 data set and 26 of these stars are present in both GC1 and GC2. A total of 86 cool stars are included in the combined 2005 data set and 50 of them are present in both GC3 and GC4. Figure 6 shows the velocity distributions for the two combined data sets. We list average radial velocities of each epoch and estimated temperatures and spectral types for these stars together with the velocities found by Figer et al. (2003) in Table 3. The mean and standard deviation of the velocity differences for stars with two velocity measurements in 1999 are 3.1 km s^{-1} and 2.5 km s^{-1}. Assuming that the errors of two velocity measurements are same but uncorrelated, we can determine 1 σ errors of the velocity measurements to be 1.8 and 1.3 km s^{-1} ($\frac{2.5^2}{2}$=1.8^2, $\frac{2.5^2}{4}$=1.3^2), in which the bigger value is for stars with only one velocity measurement (the uncertainty of individual measurements) and the smaller one is for stars with two velocity measurements (the uncertainty of the mean of two independent measurements). Applying the same method to data from 2005, we get a mean of 3.6 km s^{-1} and a standard deviation of 1.5 km s^{-1}. Therefore, 1 σ errors are 1.0 or 0.7 km s^{-1} for stars with one or two velocity measurements, respectively. The uncertainties of our measurements for the first epoch are bigger than those in Figer et al. (2003) although both studies use same sets of data. We believe that this is due to the difference in star and spectrum extraction. We used a smaller (compared to that in Figer et al. (2003)) flux threshold to find stars, and a smaller slit window to extract stellar spectra. A bigger extracting window would result in more contamination of light from near-by stars. Despite the different parameters used by two studies, good agreement can be seen between the newly derived 1999 velocities and

those found by Figer et al. (2003). The differences between the two measurements range from -1.9 to 12.3 km s^{-1} with a median difference of 7.3 km s^{-1} and a standard deviation of 2.8 km s^{-1}. We did not include IRS1NE(1) when we computed these values. Our measurements and those in Figer et al. (2003) for this source differ by 240 km s^{-1}. There must be an error, e.g. erroneous source extraction, in the measurements of Figer et al. (2003). Measurements of Figer et al. (2003) tend to have higher values than ours. This must be due to wavelength calibration. Different calibration parameters were used to calibrate wavelengths. We estimate that the systematic error caused by wavelength calibration can be up to ∼7 km s^{-1}. Finally, we used 7.3 km s^{-1} as a safe estimate of the systematic error in our measurements, which is the median difference between our measurements and values in Figer et al. (2003) for stars observed in the first epoch.

The medians and the standard deviations of stellar velocities in these data sets are shown in Table 4. The average heliocentric velocity (-7.8±10.3 km s^{-1}, 10.3=7.3×$\sqrt{2}$) corresponds to the projected motion of the Sun with respect to the local standard of rest (LSR) and the standard deviation (113.7±10.3 km s^{-1}) is a measure of the velocity dispersion of these stars. The skewness and kurtosis of individual samples are also listed. Except for the data set from GC2, values of other data sets are consistent with each other and are also consistent with the values in Dehnen & Binney (1998) and Figer et al. (2003). The different values for the data set from GC2 are probably due to a small sky area coverage of GC2 and a small size of the resulting sample.

3.2. Hot Stars

3.2.1. Spectral Variability and Radial Velocity

Based on data from the two epochs, we identified 29 hot stars. Among them, 20 stars are identified as the narrow-line type and 9 as the broad-line type He I stars. We follow the classification suggested by Paumard et al. (2001) and Tanner et al. (2006). Stars showing broad 2.058μm line emission are considered as broad-line He I stars. Their 2.058 μm line full width at zero intensity (FWZI) is usually over 1000 km s^{-1}. Stars exhibiting 2.112/2.113 μm absorption features are considered as the narrow-line He I stars. These lines are usually a few hundred km s^{-1} wide. Locations of identified objects are indicated with squares for broad-line objects and with diamonds for narrow-line objects in Figure 5. Correlation with previous identified stars (Figer et al. 2003; Tanner et al. 2006) is made based on calculated stellar coordinates. The coordinates of a star are used as the name when no published name is found.

We show multi-epoch spectra of the narrow-line stars with the He I 2.112/2.113 μm absorption feature in Figures 7. Figure 8 shows spectra of objects with broad He I 2.058μm line emission. High stellar density and large point spread functions make it difficult to subtract background spectrum from stellar spectra. The extracted sky spectra may contain emission from nearby stars, thus causing bad sky subtraction. Weak component at 2.113 μm is especially not always obvious. Emission from gas streamers (Paumard et al. 2001) at the GC sometimes makes it difficult to identify the stellar photospherical features. In order to study the acceleration, we assume that the shapes of the lines do not change on the time scale of our observations. This assumption of time consistency is supported by Figure 9, which shows the profiles of Brγ line, He I 2.112/2.113 μm and He I 2.058μm lines of two examples of the hot stars.

Of the 29 hot stars, many have radial velocity measurements by other authors (Genzel et al. 2000; Paumard et al. 2001; Tanner et al. 2006; Paumard et al. 2006). Our improved spectral resolution and multi-epoch observations provide more accurate velocity and acceleration measurements for these stars. We fit the absorption and emission features with Gaussian profiles to compute the Doppler shifts and the widths of the lines. Examples of our best fits are shown in Figure 10. The continuum components are fitted with a second degree polynomial and subtracted from the spectra before the Gaussian profile fitting. The radial velocity of a narrow-line star can be derived from either the 2.112 μm line or the 2.113 μm line in most cases. For these stars, the average of two velocities is used and the difference between two measurements is listed as the uncertainty. Some narrow-line objects show only one absorption trough in their spectra, such as IRS16SW(W). In such a case, the rest wavelength of 2.112 μm is assumed and 5% of the width (FWHM) of the Gaussian profile is taken as the uncertainty.

It is difficult to estimate stellar velocities for the broad-line stars because the emission lines of these stars generally do not have a simple Gaussian profile. The observed 2.058 μm He I line often has a distorted P-Cygni shape. Some observed profiles can be reasonably fitted with a Gaussian emission component plus a greatly blue-shifted Gaussian absorption component. Because the blue-shifted absorption component is presumably from the near side of the stellar wind, radial velocities derived from this absorption feature would significantly deviate from the real values. In order to get a good estimate of the radial velocity of a broad line star, we first use the emission component to calculate the radial velocity. Due to the fact that the blue side of emission is pulled downward by the blue-shifted absorption component, the actual line center before absorption should be bluer than the center of the Gaussian fit. Thus the derived radial velocity from the Gaussian fit serves as the upper limit to the final estimate. We acquire a second estimate of the radial velocity from the average line wavelength using the continuum-subtracted fluxes as weights. For the absorption part

of the spectral line, the absolute values of negative fluxes are used as the weights in the calculation. The resulting velocity serves as the lower limit of the estimate of the radial velocity because the presence of blue-shifted absorption makes the absolute flux weighted wavelength bluer than if no absorption were present, considering the blue-shifted absorption component is usually much weaker than the emission component and is far from the emission peak. Finally, the average value of the two estimates is taken as the final estimate of the radial velocity and a half of the difference is taken as the uncertainty.

The final radial velocities and the average equivalent widths (EW) are listed in Table 5 and 6. Unlike the cool star cases, radial velocities of some hot stars are quite uncertain due to the variation of extracted line profiles from night to night within one epoch. Big uncertainties are expected for the measurements. Therefore, we list their spectra and velocities individually. In the narrow line cases, the EW is computed from the widths of Gaussian fits. In the broad line cases, the EW is simply the integration of area under continuum-subtracted emission with the continuum level being normalized to unity. Results show that both radial velocities and line widths derived from different scans for the same object are generally consistent with each other except for in a few cases where spectral variability is important. We need to point out that velocities estimated from different features are not necessarily same. Theoretically, the Br_γ line and the He I line at 2.058 μm can also be used to estimate the stellar velocities of the narrow He I line stars. The profiles of these lines are usually complicated and result in different radial velocity estimates because of nebula emission from streamers in the region. It is also suggested that the widths and strengths of the He I emission lines are more connected with the density of the stellar wind than with the terminal velocity (Najarro 2007). In the cases of narrow He I lines, the absorption feature at 2.112 μm becomes prominent because emission in the 2.058 μm (and/or 2.112 μm) line is weak (also visually narrow). Thus the velocities computed from the 2.112μm feature can be greatly blue-shifted from the values computed from the emission features and there would be systematic errors in the velocity measurements of the narrow line objects. In some cases, this error can be up to 30 km s^{-1} (Najarro 2007). However, because estimating the velocities of the narrow He I line objects from the He I emission lines is not applicable due to the small strength of the lines, we will leave out such an investigation in this work.

Because the sky area covered by our observations varies from time to time (Figure 2), some stars in our list are not covered by all scans. Paumard et al. (2006) obtained high spatial resolution spectroimaging data of the region. We can find counterparts for many of our sources in their list. In the following, we compare our results with previous studies.

3.2.2. Narrow-line stars

We determine that 20 sources in our sample are narrow line type He I stars, including several stars which were considered featureless or broad-lined in Tanner et al. (2006). A better spectra extraction and background subtraction procedure helps to reduce contamination by light from neighboring stars. This contamination is significant in Tanner et al. (2006). The classifications of some broad line sources in Tanner et al. (2006) are ambiguous due to the weak strength of the lines.

-**IRS16NW**: Among all observed He I emission line stars, this one has the smallest projected distance from Sgr A*, only $\sim 1.0''$ away. The star is identified as an Ofpe/WN9 star (Paumard et al. 2006). Martins et al. (2007) fit the observed K band spectrum of the star and suggest that the star has just left the main sequence and is in an early evolved stage. Our spectra show a P-Cygni profile with strong blue-shifted absorption in the 2.058 μm line similar to that in Paumard et al. (2001) and Martins et al. (2007). The 2.112/2.113 μm absorption doublet is prominent in our spectra. Paumard et al. (2001) derive a radial velocity of -46 km s^{-1} for this object using the 2.058 μm line observed in 1997. Paumard et al. (2006) measure the radial velocity to be -44 km s^{-1} during the time period of 2003-2004. Both values are within the uncertainty range from our measurement.

-**IRS16C**: This star also has a spectral type of Ofpe/WN9 (Paumard et al. 2006). Its spectrum resembles that of IRS16NW except that more He I absorption is present on the blue wing of the Br$_\gamma$ line in IRS16NW (Martins et al. 2007). We detect the 2.112/2.113 μm absorption doublet in the spectrum of the object from all four nights. Our measured velocity ($\sim$100 km s^{-1}) appears consistent within 1 sigma error bars from that in Paumard et al. (2006), which is 125 km s^{-1}.

-**IRS16SW(W)**: This object was identified as a short period ($\sim$19.4 days) eclipsing binary system (Ott et al. 1999; Martins et al. 2006; Peeples et al. 2007). Its radial velocity varies in a range between $\sim$300 and 677 km s^{-1} (Ott et al. 1999; Martins et al. 2006). Its 2.112 μm line profile also varies with time, depending on which phase the system is at. We detect the 2.112 μm absorption feature in all four data sets. Our derived velocities are consistent with results in Martins et al. (2006), but are different from those in Tanner et al. (2006) (247 km s^{-1}) and Paumard et al. (2001) (354 km s^{-1}). High stellar density makes it hard to extract spectrum for this star. Therefore, its spectrum may be contaminated by light from neighboring stars, and result in big uncertainties in the estimated velocities. Three sources (IRS16SW, IRS16SSE1 and IRS16SSE2) in Paumard et al. (2006) are close to IRS16SW(W) based on their coordinates. However, none of them has an estimated radial velocity close to our measurements.

-**IRS16CC**: We confirm the identification of this star as a narrow-line star by Tanner et al. (2006). The characteristic absorption lines are observed in all four data sets. The derived radial velocities are consistent with each other and with that in Tanner et al. (2006). No obvious velocity change over the 5.8 year time span is observed for this star. Paumard et al. (2001) did not observe He I emission from this object. They claimed that the earlier identification of this star as a helium star by Blum et al. (1996a) was a mistake due to light from a nearby source - He I N2, which is 0.6″ South and 0.3″ East of IRS16CC. Our derived velocities for IRS16CC are very different from that of He I N2 in Paumard et al. (2001), implying that IRS16CC and He I N2 are probably two different sources. Our spatial resolution does not allow us to separate IRS16CC and He I N2. Paumard et al. (2006) suggest that IRS16CC is an O9.5-B0.5 supergiant, and they estimate the radial velocity of the star to be 241 km s^{-1}, which is similar to our measurements.

-**MPE 1.0-7.4**: This star was classified as a B0.5 supergiant in Paumard et al. (2006). The star belongs to IRS16 cluster of hot stars and several bright He I stars are in its vicinity. We detected the star in the second scan. Our estimate of its radial velocity is consistent with the value in Paumard et al. (2006).

-**IRS16NE**: Tanner et al. (2006) suggest that this star is a spectroscopic binary system. We detect this star in all four data sets. The radial velocity of this star changes from ∼12.8 km s^{-1} in June 1999 to ∼-60 km s^{-1} in 2005, which supports the proposal by Tanner et al. (2006). However, we did not find evidence to support the change of the line shape (the 2.112 μm line width). Paumard et al. (2006) measure the radial velocity to be -10 km s^{-1} during 2003-2004, which is within the uncertainty range of our measurements.

-**IRS33E**: This object is identified as a cool star (ID221) in Figer et al. (2003). However, no CO band head absorption feature is observed for this object in our reduced data sets. The misidentification may be due to contamination by the light from red giants in the region and bad background subtraction. IRS33E was identified as an Ofpe/WN9 star (Paumard et al. 2006). Martins et al. (2007) show that the K band spectrum of IRS33E resembles that of IRS34W, IRS16NW and IRS16C except that the Br$_\gamma$ line of IRS33E has a complicated line profile. The 2.112/2.113 μm doublet absorption feature can be seen clearly in our spectra. Our observations show that the radial velocity of this object ranges ∼150 km s^{-1} and ∼110 km s^{-1} between 1999 and 2005, and does not change significantly over the 5.8 year time span. Paumard et al. (2001) computed the radial velocity of the object (IRS33SE) using the 2.058 μm emission line which is strongly affected by diffuse emission from ISM. They had a much higher velocity ∼258 km s^{-1}. Paumard et al. (2006) reports the radial velocity of IRS33E to be 170±20 km s^{-1} between 2003 and 2005, still higher than the values we found.

-**IRS34W**: This object was identified as a narrow-line type He I star by many investigators (Paumard et al. 2001; Ott et al. 2003; Paumard et al. 2003; Trippe et al. 2006). Paumard et al. (2006) identified its spectral type to be Ofpe/WN9. The star is also believed to be a LBV candidate (Paumard et al. 2001; Trippe et al. 2006) based on its changing K band magnitude with $\Delta K \sim 1.5$. Despite the star's highly variable K magnitude, the spectrum of the star does not show any variability. Paumard et al. (2001) point out that the source consists of two stars (34E and 34 W) of similar brightness. Our angular resolution is not high enough to separate them. Trippe et al. (2006) suggest that the star is not a LBV but a star with a spectral type between O supergiant and LBV. Trippe et al. (2006) showed that the stellar spectrum has a clear P-Cygni profile in 2.058 μm and 2.112 μm He I lines. A broad Br$_\gamma$ line with a blue-shifted shoulder can also be seen in its spectrum. Our spectra from GC1 and GC3 are similar to each other and to those in Trippe et al. (2006) and Martins et al. (2007). Single peak absorption is observed in the 2.112 μm line. Tanner et al. (2006) did not detect the 2.112/2.113μm absorption feature, possibly due to bad sky subtraction. The velocities derived from the absorption feature at 2.112 μm in our spectra are consistent with each other, although they are different from that in Paumard et al. (2001), which was derived from the 2.058 μm He I line. Paumard et al. (2006) measure the radial velocity of the star again and find a value similar to our result.

-**A21**: This star is located at the center of the eastern cavity between the northern arm and the eastern arm. The 2.112μm line absorption is quite strong. We detected the line in all four data sets, although spectrum from GC2 is noisier than those from other scans. Absorption of the 2.113 μm line is generally missing in our spectra. The star does not show obvious radial velocity shift over the 5-year time span.

-**ID308**: This star was identified as a cool star in Figer et al. (2003). Our multiple night observations show that it is a narrow He I line star. The CO absorption features present in the raw spectra are greatly reduced after the subtraction of sky background emission. This suggests that the CO feature is coming from the background cluster of cool stars. Derived radial velocities are consistent with each other. The position of the star matches that of IRS1E (E67) in Paumard et al. (2006), which is classified as a B1-3 supergiant. Paumard et al. (2006) found that the radial velocity of the star is $\sim 8 \pm 20$ km s^{-1}, higher than our measurements.

-**MPE+1.41-12.2**: We detect the He I absorption feature in this object in all four data sets. Both 2.112 and 2.113μm lines are detected in this object. Spectrum from GC1 is ~ 25 km s^{-1} more red shifted than those from GC3 and GC4. The radial velocity from GC2 data set is very close to those from GC3 and 4, which may be due to the uncertainty of our measurements. Our measurements are within the uncertainty range of the value

($\sim 153 \pm 50$ km s^{-1}) by Paumard et al. (2006).

-**IRS6W**: This narrow-line object is only observed in our first scan because it is outside of fields of other scans. It seems that its coordinates in Tanner et al. (2006) are mixed with those of 6E. 6E, identified as a WC9 star by Krabbe et al. (1995), does not show any obvious stellar photospheric feature in our observations. Paumard et al. (2001) attribute observed broad 2.058 μm emission to nearby helium streamers and suggest that the earlier WC9 classification was a misidentification. We do not observe broad 2.058 μm line mission, but we detect 2.112/2.113 μm absorption doublet to confirm IRS6W to be a narrow He I star. We do not find this star in the list of Paumard et al. (2006).

-**IRS26**: The He I absorption feature in the spectrum of this star is detected in all four slit scans. Both 2.112 and 2.113 μm lines can be seen in these spectra. The derived velocities are consistent with each other and indicate no relative acceleration during 1999-2005. Paumard et al. (2006) estimate a similar radial velocity for this star, and they suggest that the star is an O9 or early B type supergiant.

-**AFNWB**: Tanner et al. (2006) identify this object as a broad line He I star. However, we did not observe the broad line emission at the position of the star. We believe that the misclassification is due to a nearby broad line source AFNW, which is $\sim 0.6''$E and $0.4''$S of this star. AFNWB lies on the west edge of our scanning field. We have only one measurement of its radial velocity. Paumard et al. (2006) do not include this star in their list.

-**G1138**: The same star is named as BSD WC9B in Blum et al. (1996a). In our spectrum, the star shows weak and narrow absorption at ~ 2.112 μm. We do not agree with Tanner et al. (2006) on classifying this star as a broad line object. No obvious 2.058 μm emission is observed at the location of the star in our data set. Weak 2.058 μm line emission in the Tanner et al. (2006) spectrum suggests that the confusion may be caused by bad sky background subtraction.

--**8.91-6.76**: Tanner et al. (2006) identified this star as a narrow line He I object. They mixed the star with BlumWC9, which was identified as a WC9 Wolf-Rayet star by Blum et al. (1995). We construct the image for the entire field of our observations from our slit scan data and compare the resulting image with that of Martins (2007). The comparison shows that BlumWC9 and -8.91-6.76 are different objects. BlumWC9 is the faint object $\sim 0.4''$ NE of -8.91-6.76 and is probably buried in the light of -8.91-6.76 in our observations. Our observations confirm that -8.91-6.76 is a narrow line object. The 2.112/2.113 μm doublet absorption feature is prominent in our K band spectrum of the star. Our derived stellar velocity and line width agree with the results in Tanner et al. (2006).

3.2.3.   Broad-line stars

We identify 9 objects to be broad line He I star candidates. Their spectra show broad 2.058 μm or 2.112/2.113 μm line emission.

-**IRS13E**: IRS13E is a compact stellar cluster containing at least three bright stars (Paumard et al. 2001; Schödel et al. 2005; Paumard et al. 2006). It has been suggested that IRS13E is the remnant of a massive cluster falling into the GC from the outer region (Maillard et al. 2004; Schödel et al. 2005). It is also suggested that IRS13E contains an IMBH with a mass $\geq 10^4 M_\odot$ stabilizes the inspiraling cluster and holds the massive cluster together against the tidal force of Sgr A* during the infall. Paumard et al. (2006) carefully analyze proper motions of stars that are assumed to be members of IRS13E. They argue that the presence of an IMBH is hindered by the ambiguous cluster membership of a few stars in the analysis of Maillard et al. (2004) and Schödel et al. (2005). Our data have relatively low angular resolution compared to those AO observations. IRS13E is present as one single broad line He I source in our observations. This classification is consistent with previous studies (Najarro et al. 1997; Paumard et al. 2001). Our spectra of four nights show similar distorted P-Cygni profiles for this object. Blue-shifted absorption components can be seen clearly. The wavelength shift between profiles of the two epochs is obvious. The cross-correlation fitting gives a $\sim$35 km s^{-1} difference for the radial velocity at the two epochs. None of IRS13E members in Paumard et al. (2006) has a similar radial velocity as we observed.

-**IRS7W**: We detected strong and broad emission in He I 2.058, 2.112 μm and Br$_\gamma$ lines in GC1, GC2 and GC3. P-Cygni profiles with shallow blue-shifted absorption of the 2.058 μm line can be seen clearly in these spectra and resemble each other. Our three measurements of the radial velocity indicate that the line-of-sight acceleration of the star is small. This star is classified as a WC9 star by Paumard et al. (2006). However, IRS7SW in their list of stars seems closer to our source in coordinates. IRS7SW has a type of WN8. Both two stars have a radial velocity ($\leq$-300 km s^{-1}) more negative than our measurement ($\sim$-190 km s^{-1}).

-**GCHe2**: GCHe2 (Tamblyn et al. 1996) is also named as IRS 9W and is classified as a broad He I line star by Paumard et al. (2001). It is then identified as a WN8 star in Paumard et al. (2006) and shows strong He II lines (Martins et al. 2007). The object shows broad distorted P-Cygni profile 2.058 μm line emission in our spectra. The overall line profiles and wavelength ranges of emission match each other fairly well with a $\sim$50 km s^{-1} shift. Our measurements of the radial velocity of the star have a big variance, which can be due to the complexity of the line shape and the uncertainty associated with the method to estimate the velocity in the broad line cases. Paumard et al. (2001) estimate that the

radial velocity to be 221 km s^{-1}, and the new measurement by Paumard et al. (2006) is ~140 km s^{-1}.

-**ID415**: We use the cool star designation from Figer et al. (2003) for this object although IRS7E2 seems to be very close to this star in location (Paumard et al. 2001). IRS7E2 was identified to have a WN8 spectral type (Paumard et al. 2006). We detect broad 2.058 μm line emission from the star in three data sets. The line profiles in these observations match each other very well and show no relative velocity shift between them. Spectrum in Martins et al. (2007) shows strong Br$_\gamma$ line emission with a width similar to that of 2.058 μm He I line, which is not shown in our data. This object also shows strong CO absorption. It is possible that light from multiple stars falls into our big beam simultaneously. The CO and He I features do not vary with time indicating that the stars do not form a binary system.

-**AFNW**: AFNW is identified as a WN8 type star by Paumard et al. (2006) and shows broad emission in He I lines (2.058 and 2.112 μm) and Brγ line in our GC1 spectrum. This star is also identified as a broad line object by Paumard et al. (2001). Our measurement of the radial velocity agrees with that in (Paumard et al. 2001, ~159 km s^{-1}). The measurement by (Paumard et al. 2006, ~70 km s^{-1}) is much smaller.

-**ID180**: ID180 is discovered by Paumard et al. (2001) as a broad line object. The radial velocity was measured to be ~198 km s^{-1}. Paumard et al. (2006) measure the velocity again and get a value ~-230 km s^{-1}. Our estimate of the velocity is ~-16 km s^{-1}. It indicates that the measurements are quite uncertain. The star is identified as a WC9 star by Paumard et al. (2006).

-**AF**: Paumard et al. (2001) point out that this star is much brighter than other broad line objects in their list and suggest that a compact binary system may be present. Additional evidence is provided by Ott et al. (1999), who find that the K band photometry of this star shows some indication of time variability. Najarro et al. (1994) modeled observed spectrum from the source with unified atmosphere/wind models and concluded that the star was not a classical Wolf-Rayet star because no other high excitation lines were detected. They suggested that the star is an Ofpe/WN9 type blue supergiant based on model parameters, which is consistent with the classification by Paumard et al. (2006). Martins et al. (2007) point out that AF has much broader lines compared with many other Ofpe/WN9 stars and suggest that AF has a stronger wind and is in a more evolved stage. In our data set, the AF star shows broad emission in 2.058 μm, 2.112 μm He I and Brγ lines that are not related to ISM. The 2.058 μm line emission has a typical P-Cygni profile with a strong emission peak and a shallow blue-shifted absorption trough. We fit the emission peak with a single Gaussian component to derived the stellar radial velocity, which is similar to that in Tanner et al. (2006), but ~50 km s^{-1} higher than in Paumard et al. (2001) and ~80 km s^{-1}

higher than in Paumard et al. (2006).

-**IRS15SW**: IRS15SW is classified as WN8/WC9 by Paumard et al. (2006) because of C lines present in its K band spectrum (Martins et al. 2007). Our observations show a broad emission line with a regular P-Cygni profile at ∼2.058 μm. Radial velocity measurements of this object at two epochs are similar to each other, but less bluer than that in (Paumard et al. 2001, ∼179 km s^{-1}) and (Paumard et al. 2006, ∼-180 km s^{-1}). The spectra indicate a small line-of-sight acceleration during the time between two epochs.

-**IRS9S**: We detected this star in all four data sets. Only one spectrum shows weak 2.058 μm emission. All four spectra show broad emission at ∼2.112 μm. Thus, we use this part of the spectra to estimate the radial velocity of the star. All but one estimated velocities are consistent with other, but much higher than the measurement in Paumard et al. (2006). The star is identified as a WC9 star.

Due to the high stellar density in the region and the presence of ISM streamers (Paumard et al. 2001), contamination from neighboring stars and ISM is large. In our study, we carefully choose pixels for stars and background during background subtraction and stellar spectrum extraction to avoid as much contamination as possible. we use both spatial and spectral information to identify different sources. This helps us to identify many sources which were not found by Figer et al. (2003) and Tanner et al. (2006). However, the spatial resolution of our observations is still low and is not able to resolve many sources into individual stars in the crowded region. In at least one case (ID415), we find characteristic spectral features of cool and hot stars in the co-added spectrum at the same time. Thus ID415 is included in both the cool and hot samples. We also find one case (IRS13E) in which both narrow absorption and broad emission features are present at the same time. These features must come from different stars which lie closely on the sky. This situation can only be improved by future high spatial resolution observations. Finally, our radial velocity measurements of 7 of 20 narrow line stars and 2 of 8 broad line stars detected in the first epoch have similar values as in Tanner et al. (2006). We also found that 11 narrow line stars have radial velocities similar to the values in Paumard et al. (2006). The differences between these measurements are less than 40 km s^{-1}, roughly the median value of the uncertainties of the radial velocities in Paumard et al. (2006). However, the differences between our measurements and those in Paumard et al. (2006) for broad line stars are usually bigger than this value. Low spectral resolution of data in Paumard et al. (2006) and low spatial resolution of our observations should be the major causes for the differences. Different spectral resolutions of the observations and the large intrinsic line widths of the stars can result in big differences and uncertainties in the line centers found through Gaussian profile fitting. The results suggest that large uncertainties are present in the radial velocity measurements and high sensitivity

and high resolution observations are required to improve this situation.

3.3. Distribution

We show stellar surface densities and radial velocity dispersions of the late type stars as functions of the projected distance (r_P) from Sgr A* in Figure 11. The results from the current data and from the published data in Figer et al. (2003) are indicated with solid lines (filled circles) and dashed lines (open circles), respectively. These plots only include those stars with a projected Galactic radius $r_P<0.4$ pc ($\sim$10 arcsecs) so that the resulting data set is complete in the sense that it covers a circular region on the sky with its center at Sgr A*, and the magnitude limit of the sample is K$\simeq$13. Same bins are used to create the surface density plots and the corresponding velocity dispersion plots. Our cool star surface density is consistent with previous results (Figer et al. 2003) by showing two bumps ($r_P \simeq 0.07$ and 0.3 pc) and one low density region at $r_P \sim$0.15 pc. The difference between two curves can be attributed to the different sizes of the two samples. The low surface density at $r_P \sim$0.15 pc shown by both curves indicates the presence of a central "hole" of late type stars. Such a hole is also supported by CO bandhead strength mapping and infrared photometric observations (Sellgren et al. 1990; Haller et al. 1996; Genzel et al. 1996; Schödel et al. 2007). Schödel et al. (2007) found an under-density of stars at 5" and over-densities at 3" and 7" based on photometric data. These results are similar to what we found. Beside the surface density profiles, the velocity dispersions of late type stars are quite flat in the observed region. No obvious velocity dispersion increase toward the GC is supported by the data. Monte Carlo simulations suggest that a central low stellar density region is needed to explain the observed projected number density and flat velocity dispersion curves (Figer et al. 2003). Mechanisms which have been suggested to explain the formation of such a "hole" include stellar collision (Lacy et al. 1982; Genzel et al. 1996; Alexander 1999; Bailey & Davies 1999), atmospheric striping (Alexander & Livio 2001), atmospheric heating (Alexander & Morris 2003) and dynamical ejection (Miralda-Escudé & Gould 2000; Figer et al. 2003). The hump at the $r_P \sim$0.07 pc is a surprising result because one would expect that these mechanisms causing the central "hole" would affect all stars in the region. This hump is probably due to small number statistics and the stars observed at the small projected radii are actually in front of or behind the central "hole". Due to the small area of the first bin, a small fluctuation in the star count can result in a big surface density. The velocity dispersions of late type stars are quite flat in the observed region. No obvious velocity dispersion increase toward the GC is supported by the data.

The surface density and the velocity dispersion of the early type stars are shown as

functions of the projected distance from Sgr A* in Figure 12. The surface density decreases with the projected distance with a local peak at r_P ~0.1 pc due to the IRS16 cluster. Observations suggest that early type stars between the projected distance r_P=1$''$ and 12$''$ from Sgr A* belong to two disk-like structures rotating about the GC and at least one disk is nearly edge-on (Levin & Beloborodov 2003; Genzel et al. 2003).

The velocity distributions of both the late type and the early type stars are quite symmetric as shown by Figure 13. We fit the velocity distributions with Gaussian functions, and the fitted widths (standard deviations) are indicated with the statistical quantities of the distributions. A 20 km s^{-1} bin size is used to make the histograms before doing Gaussian fitting. We note that the fitting results are not sensitive to the bin size between 16 and 26 km s^{-1}. The results show that standard deviations from the two methods are different. For the late type stars, the statistical standard deviation of the observed velocities is close to 110 km s^{-1}, while Gaussian fitting yields a value of ~87 km s^{-1}. Velocities of the early type stars also have significantly different values for statistical and fitted standard deviations. Moreover, both velocity distributions skew slightly to the left (more negative velocity). A positive kurtosis of the late type star velocities indicates the number of the stars with the smallest and/or highest velocities is greater than the value expected by a normal distribution with the same mean and variance. A negative kurtosis suggests a large number of early type stars having intermediate velocities. Monte Carlo simulations of a Gaussian-distributed velocity sample with a mean of -10 km s^{-1} and a standard deviation of 110 km s^{-1} show that there is ~7% probability that the fitted standard deviation would fall below 87 km s^{-1} when the sample size is equal to 97, and this probability drops down to ~4% when the sample size is increased to 123. The simulations suggest that the smaller standard deviation found by our Gaussian fitting procedure is not entirely due to the small size of our sample, and that the observed velocities deviate from Gaussian distributions. The D′Agostino-Pearson K^2 test based on the skewness and the kurtosis (D'Agostino et al. 1990) also suggests that our Gaussian fittings are poor, and that both velocity distributions deviate from Gaussian distributions. The probability of the observed velocity distribution being normal is ~20% (~60%) for the late (early) type stars.

The deviation from normality in the case of the late type stars is probably due to our method of finding and identifying stars. Our star-finding procedure tends to reject faint stars close to bright ones and our star-identifying procedure also tends to throw away stars with spectra of low s/n in order to compute correct wavelength shifts. Therefore, our statistics are dominated by the brightest stars in the region, which include many intermediate-mass (3M$_\odot$ <M$_*$ < 8M$_\odot$) AGB stars that are found in the central parsec of the Galaxy (Genzel et al. 2000, 2003). These stars have much shorter lifetimes (up to a few 10^8 yrs) compared with low-mass (M$_*$ < 3M$_\odot$) stars, which lives for a few 10^9 years. These two

populations of stars may have different velocity distributions due to their different ages and relaxation times. The two-body relaxation time for a solar mass star in the GC is of the order $\sim 10^9$ yrs, which is comparable to its age, while the relaxation time scales as $M_*{}^{-1}$ and it is usually longer than the lifetime of an intermediate-mass or massive star (Genzel et al. 2000; Merritt & Szell 2006). We cross-correlate our late type stellar sample with that provided by Genzel et al. (1996), who divides the stars into three K band magnitude groups: K≤10.5, 10.5≤K≤12 and K≥12. In total, 63 stars are present in both samples. The comparison shows a substantial change in the luminosity function from 25:53:120 in Genzel et al. (1996) to 19:18:26 in our case. A higher percentage of bright stars are present in the sub-sample, supporting our hypothesis. Thus our observed velocities of the late type stars can have a non-Gaussian distribution even the velocities of the low mass late type stars are normally distributed. In addition, the "missing" stars in the central hole may also drive the overall velocity distribution of the late type stars away from a normal distribution. In the case of the early type stars, the intrinsic velocity distribution is probably non-Gaussian due to the short ages.

3.4.   Rotation and Acceleration

Radial velocities of the identified stars are plotted as a function of the projected distance from the Sgr A* in Figure 14. Two plots are for cool (left) and hot (right) populations, respectively. We also plot ideal circular orbital velocities (solid lines) and escape velocities (dotted lines) around a dominating central object with a mass of 3.5×10^6 M$_\odot$ as comparison. Although several stars have velocities beyond the limits of circular orbital motions, radial velocities of most stars are within the range allowed by circular orbits. The speed of IRS9 exceeds the escape velocity at its projected distance. The star is probably ejected from the central cluster, as suggested by Reid et al. (2007).

We plot radial velocities of the cool stars against their Right Ascension and Declination offsets from Sgr A* (Figure 15). No correlation is indicated by these plots, which leads us to conclude that there is no, or a very small, systematic rotation for the late-type population. Figure 16 shows the average radial velocities of hot stars verse their Right Ascension and Declination offsets from Sgr A*. The plots include both the narrow- (filled circles) and broad-line (open circles) stars. A correlation between the radial velocity and the Declination offset can be seen for the hot stars (right plot). This correlation is especially evident for the broad emission line stars. Most hot stars distribute along a diagonal from the upper left quadrant to the lower right quadrant through Sgr A*, and the stars north of Sgr A* have red-shifted velocities and the stars south of Sgr A* have blue-shifted velocities. This result

confirms a systematic rotation for hot stars, consistent with other observations (Genzel et al. 2000; Paumard et al. 2001, 2006). It has been suggested that hot stars at the GC form one or two disk-like structures (Genzel et al. 2000; Paumard et al. 2001; Levin & Beloborodov 2003; Genzel et al. 2003; Paumard et al. 2006; Lu et al. 2007). Our observations support the existence of disk-like structure, however additional information about stellar proper motions is needed to construct the 3-D distribution of hot stars and study other properties of the disk-like structures.

Using data sets from the two epochs, we examine acceleration of stars in the region over this period. The changes of the radial velocities of the stars that are observed in both 1999 and 2005 are plotted against the projected Galactic distances in Figure 17. No correlation is apparent between the velocity changes and the projected distances from the Galactic center. To compute the velocity changes of the observed hot stars, we shift and cross-correlate spectra of the hot stars from two epochs to compute the best velocity shifts to avoid big uncertainties caused by low quality of spectra and large line widths. The pixel size of our re-sampling grid is used as uncertainties. In a few cases, when the relative wavelength shift found by cross-correlation is not good due to the variation of the line shape, and line features are obviously misaligned, we adjust the spectral shift manually so that the overall line profiles from different observations are aligned with each other, and the difference between the shift found by cross-correlation and the manual shift is used as uncertainties.

It can be shown (Appendix A) that for edge-on circular orbits the velocity change of a star at a projected radius R_0 follows a relation:

$$\Delta v = -[s_1 \frac{GM}{R} \frac{\sqrt{R^2 - R_0^2}}{R^2} \tau + s_2 \sqrt{(\frac{GM}{R})^3} \frac{R_0}{2R^3} \tau^2], \tag{1}$$

where G is the gravitational constant, M the mass of the central object and τ the time between two observations. The signs of two terms (s_1 and s_2) are determined by the direction of rotation and the location of the star with respect to the tangent point. This relation assumes that all stars are in circular orbits. This assumption is not necessarily true since the stellar orbits are generally not circular (e=0), but tend to have high eccentricities (Bahcall & Wolf 1976). Nevertheless, the derived formula helps us gain some insights about the stellar system we observe. It can be proved that for each projected distance there is a maximum radial velocity change allowed by the formula. The maximum velocity change is plotted as a function of the projected distance in Figure 17. The curve is for a central object with a mass of $3.5 \times 10^6 M_\odot$ and a time separation of 5.8 years between two velocity measurements. The plots show that at least one cool star and many hot stars, in our sample, show a velocity change larger than the maximum value allowed by circular rotations. IRS7 shows the biggest velocity change in our plot for cool stars and the value exceeds the maximum

velocity change allowed at its projected distance from the GC. This was not reported by previous observations because of relatively low spectral resolutions. Ott et al. (1999) discussed the magnitude change of IRS7 and found that the stellar light curve reached a temporal minimum in 1998. These authors suggested that IRS7 is a red supergiant on the asymptotic giant branch (AGB). Thus the large velocity change we observed may be related to the stellar surface activity during the AGB phase. Follow-up observations are needed to investigate such a possibility. Among all observed hot stars, IRS16W(SW) and IRS16NE stand out with large velocity changes over the 5.8 year period. This is consistent with their identities as binary systems. GCHe2 also has a large velocity change which may be an indication of the spectral variability of the star. Our data show that the radial velocity change generally is bigger for hot stars than for cool stars, suggesting that the motions of the early-type stars deviate greatly from circular orbital motions.

3.5. Enclosed Mass

We try to estimate the enclosed mass in the inner parsec of the GC using different projected mass estimators. The classical Bahcall-Tremaine (BT) estimator assumes that the velocities of the particles in the system are isotropic and all the mass of the system is in a central point (Bahcall & Tremaine 1981). It predicts that the mass enclosed within a radius R_0 is:

$$M_{BT} = \frac{16}{\pi G N} \sum v_r^2 R_P. \tag{2}$$

Where G is the gravitational constant, N the number of stars, v_r the line-of-sight velocity, R_P the projected radius from the center, and the summation is over all stars within the projected radius, R_0. Equally weighted mass estimators are used in our study because, as pointed out by Bahcall & Tremaine (1981), theoretically every detected star carries the same amount of information about the enclosed mass. The weighted mass estimators implicitly assume some stars carry more information than others thus the result is biased by those stars with bigger weights. Such as in Figer et al. (2003), stars with bigger weights are from the overlapped region which was covered by two scans (GC1 and GC2) in 1999. Since the region covered by GC2 is much smaller than that covered by GC1 and is asymmetric to Sgr A* (Figure 2), the calculated enclosed masses are biased by stars in the smaller region. The resulting enclosed mass is displayed as a function of the projected radius from the Sgr A* in Figure 18 (left panel). In the calculation, R_0 is the size of a circular region which is centered at Sgr A* and is entirely contained inside the area covered by the combined data set. The summation only includes the stars inside the circle to avoid the bias caused by the asymmetry of the entire observed region. The largest possible R_0 in our case is ~ 0.4 pc. During the calculation, we

use the average velocity of each star in the sample for v_r if multiple velocity measurements are available. We do not include two stars, IRS9 and -3.03+1.35, in the calculation because of their extremely large radial velocities ($v_r >$ 300 km s^{-1}). The median velocity ($\sim$ -10 km s^{-1}) of the resulting sample of 76 stars is subtracted from v_r to remove effects of the systematic velocity shift before computing the enclosed masses. Our calculation indicates that the mass enclosed within a projected radius of 0.4 pc is $\sim$3.3$\pm$0.6$\times$10^{6}M$_\odot$. An alternate version of the BT estimator assumes that the mass is distributed like the light, but still assumes isotropic motions (Heisler et al. 1985). In this case, exactly twice amount of mass is needed to bind the system.

When we have no knowledge about the velocity anisotropy of a system, we can use a more traditional mass estimator based on the Virial Theorem (VT), which also assumes that the mass of the system is at the center (Bahcall & Tremaine 1981; Merritt 1987), but it does not assume any degree of velocity anisotropy. The VT mass estimator predicts that the central BH mass of a spherical system is:

$$M_{VT} = \frac{3\pi}{2G} \frac{\sum v_r^2}{\sum R_P^{-1}}. \tag{3}$$

Placing all the mass in the center is equivalent to deriving the minimum mass that can bind the system (Merritt 1987). Therefore, the VT mass estimator puts a lower limit on the BH mass. An alternative form of the VT mass estimator is (Limber & Mathews 1960):

$$M'_{VT} = \frac{3\pi N}{2G} \frac{\sum v_r^2}{\sum R_{ij}^{-1}}, (i < j). \tag{4}$$

Here R_{ij} is the projected distance between individual stars in the region. This mass estimator assumes that the mass distributes in the same way as stars in the system. It requires more mass to bond a system if the mass distributes evenly, thus M'_{VT} equivalently puts an upper limit on the estimated BH mass. The results from these two equations are shown in Figure 18 (right panel) with the filled circles for the case with all mass in the central point and the open circles for the case in which mass follows light. The ratios between two sets of estimated masses range between $\sim$2.0 and $\sim$3.0. The best estimate would be a value between 2.6$\pm$0.4$\times$10^6 M$_\odot$ and 5.8$\pm$1.7$\times$10^6 M$_\odot$, which is consistent the result using the classical BT estimator. Using these values, we estimate that the enclosed black mass within 0.4 pc of Sgr A* is 3.9$\pm$1.1$\times$10^6 M$_\odot$. This value is consistent with previous results using a single star's 3D orbit (3.7$\pm$1.5$\times$10^6 M$_\odot$ Schödel et al. 2002; Ghez et al. 2003, 2005) or using the proper motions of late type stars (3.0$\pm$0.5$\times$10^6 M$_\odot$ Genzel et al. 2000), so the BT estimator gives a good estimate after all. We discard the value estimated for the case of uniformly distributed mass (the alternate version of the BT estimator) because the value is outside of the range set by the Virial Theorem.

4. Discussion

4.1. Projected mass estimators and stellar velocity distributions

We estimate the mass of the central object using different projected mass estimators. Although our estimate is consistent with the values using the stellar orbits (Schödel et al. 2002; Ghez et al. 2005), we should be aware of the weakness of such a statistical method. Projected mass estimators largely rely on the theoretical work which usually assumes a certain degree of anisotropy. In the Virial Theorem case, the estimators are derived from systems which are well sampled in both space and phase. Observations are inevitably incomplete in this sense, particularly in the GC case, where observations are limited by the size of sky coverage and non-uniform extinction across the field of observations. The observed stars will not make a complete sample of the dynamical system. This under-sampling will result in an under-estimate of the enclosed mass.

The velocity distribution of a stellar population contains information about how the corresponding sample evolves under gravitational influences of the surrounding environment or whether the population is dynamically relaxed. The velocity distributions of late and early type stars in the inner parsec of the GC both are approximately symmetric in shape (skewness≃0.0), but they both deviate from a Gaussian distribution. Although we expect that the late type sample has a more relaxed velocity distribution because of the comparable lifetimes and relaxation times of these stars, even relaxed populations can have non-Gaussian velocity distributions, particularly in the vicinity of a black hole (e.g. van der Marel 1994). Moreover, previous studies suggest that multiple populations of late type stars are present in the observed region (Genzel et al. 2003, and references therein). The overall velocity distribution of the late type stars may not be a consistent one. Depending on the nature of the central "hole" of late type stars, the cluster of late type stars in the GC may deviate from a spheroid and the observed radial velocity distribution deviates from the real distribution.

4.2. Spectral types of GC hot stars

We show that stellar He I features at 2.112/2.113 μm and 2.0581 μm can be used to divide hot He I stars in the GC into two groups: narrow-line and broad-line. This method is more accurate than the one using only the 2.0581 μm feature because the absorption feature at 2.112 μm is less affected by emission from diffuse interstellar gas. However, we are not very clear about the connection between this morphological classification and the spectral types of He I stars. Many works have been devoted to identifying the spectral types of GC He I stars (Hanson & Conti 1994; Hanson et al. 1996; Morris et al. 1996; Tamblyn et al. 1996;

Figer et al. 1997; Najarro et al. 1997; Paumard et al. 2001, 2006). These studies show that stars of a large variety of spectral types emit He I 2.058 μm line. These spectral types include WC, late WN, Ofpe/WN9, LBV, Oe/Be. Despite the complexity of the situation, a correlation seems to exist between the spectral types and line widths of He I stars. Paumard et al. (2001) suggested that GC He I stars can be loosely identified as LBV (narrow line objects) or WR (broad line objects) based on their spectral morphologies and K band magnitudes. Table 7 lists spectral types of some He I stars from literatures (Paumard et al. 2006) and the table clearly shows a tendency of identifying narrow line objects to be Ofpe/WN9 stars and broad line objects to be late type Wolf-Rayet stars. The Ofpe/WN9 and LBV stages are considered to be close to each other on the evolutionary track of massive stars because stellar spectra at these two stages have many similarities (Martins et al. 2007). Such a tendency is consistent with evolutionary models of massive stars in which stars lose a large amount of mass during the early stages of evolution. More evolved stars tend to have higher surface gravity and stronger radiation field because of their smaller sizes and high surface temperatures due to exposed helium-burning cores. Such models predict that massive stars of later types generally have relatively faster winds. However, this simple solution does not stand in some cases. Our spectrum of AF shows strong and broad emission in multiple lines, but it is identified as an Ofpe/WN9 by Paumard et al. (2006). Similar discrepancy also happens in the case of ID415. It seems that both stages (Ofpe/WN9 and WC9) can have either fast ($>$1000 km s^{-1}) or slow ($<$1000 km s^{-1}) winds. Further studies are needed to better constrain the spectral types of these stars.

4.3. Origin of GC hot stars

The presence of a large number of He I stars in the GC poses a challenge to understanding the origin of these stars and the star formation history in the GC. The correlation between the radial velocities of the hot stars and their projected distances (Declination offsets) from Sgr A* supports that all GC He I stars belong to one or two disk like structures which rotate about the gravitational center. Previous studies of stellar dynamics at the GC suggest that hot stars belong to two counter-rotating disks in two planes that are at a large angle from each other (Paumard et al. 2006). New analysis indicates that there is only one disk Lu et al. (2007). Our observations do not allow us to make conclusive remarks on where one or two such disks are present. Such conclusions need additional information, such as proper motion velocities, about the stars.

In any case, the similar ages of the two types of stars suggest that hot stars have formed in one or two star formation events ∼6 Myr ago (Genzel et al. 1996, 2000; Paumard et al.

2001, 2006; Lu et al. 2007). Paumard et al. (2001) suggest that the stars formed from the same disk of gas and dust around the dynamical center. Due to tidal forces or/and other unknown effects, radial structures developed in the disk during the star formation event with the most massive stars in the outer ring, less massive stars in the middle cluster. This scenario can explain why all these stars are roughly along the same diagonal in Figure 16 (right) and have similar ages. The model is also consistent with the spatial distribution of broad line objects and narrow line objects. However, it cannot explain why planes of two disks form a big angle between them as shown by Paumard et al. (2006) since we would expect two disks to have similar orientations if these structures have formed from the same disk of gas and dust. Alternatively, stars could form from the different dynamical structures of gas and dust, such as multiple molecular clouds originally orbiting the GC. This model can avoid difficulties associated with differences between two stellar disks, but it needs to explain why stars were forming at about the same time in multiple structures. Another competitive formation scenario is the inspiraling cluster model in which stars are formed elsewhere outside the central region of the GC and migrate inward due to dynamical friction. Such a model has been proved to be unlikely because the model predicted surface density and total mass of the disk differ significantly from observations (Paumard et al. 2006). It is also very unlikely that two separate cluster inspiraling events happen at the same time.

5. Summary

We report slit scan observations toward the GC in the two epochs separated by ~5.8 years. We identify stars based on spectroscopic features at 2.2395 μm CO band heads, 2.112/2.112 μm He I line and 2.058 μm He I line. As a result, 123 cool, late type (mostly red giants), 20 narrow line and 9 broad line early type He I stars are detected in our combined data set. We measure the radial velocities of these stars in the two epochs and their velocity changes between the two epochs. The velocity dispersion and the surface density distribution of the late type stars support that a cavity of low stellar density is present at the center of the system, which has been suggested by previous IR photometries and model simulations. Using projected mass estimators, we estimate that the mass of the central black object is $\sim3.9\pm1.1\times10^6$ M$_\odot$. No systematic rotation about the central black hole is indicated by our observations for the late type stars. A systematic rotation exists for the early type stars with the stars north to Sgr A* relatively blue-shifted and the stars south to Sgr A* relatively red-shifted. The measured velocity changes of many early type stars exceed the maximum values allowed by edge-on circular orbital motions around a central object with 3.5×10^6 M$_\odot$, suggesting that these stars may move in high eccentricity orbits.

A. The radial velocity change for a circular orbit system

A star of mass m moves at a speed v in an edge-on circular orbit with a radius R around a central object of mass M. We have:

$$v = \sqrt{\frac{GM}{R}} \tag{A1}$$

If the projected distance is R_0, we have:

$$cos(\phi) = \frac{R_0}{R}, \qquad sin(\phi) = \frac{L}{R}. \tag{A2}$$

Where $L = \sqrt{R^2 - R_0^2}$ is the distance between the star's location to the tangent point. The radial velocity of the star is:

$$v_r = v cos(\phi). \tag{A3}$$

After a small time span τ, the star moves $\Delta\phi$ in the orbit. We have:

$$v_r' = v cos(\phi + \Delta\phi). \tag{A4}$$

with

$$\Delta\phi = \frac{v\tau}{R} = \sqrt{\frac{GM}{R^3}}\tau. \tag{A5}$$

The change of the radial velocity is:

$$\Delta v_r(R_0, L) = v_r' - v_r = v[cos(\phi + \Delta\phi) - cos(\phi)] \tag{A6}$$

$$\simeq -v[sin(\phi)\Delta\phi + \frac{1}{2}cos(\phi)\Delta\phi^2] \tag{A7}$$

$$= -[s_1 \frac{GM}{R} \frac{\sqrt{R^2 - R_0^2}}{R^2}\tau + s_2\sqrt{(\frac{GM}{R})^3}\frac{R_0}{2R^3}\tau^2]. \tag{A8}$$

Since all ϕ, $\Delta\phi$ and v can be positive or negative, two terms in Eq. A6 can be either positive or negative. Thus s_1 and s_2 are used to represent the signs of two terms. The absolute change of the radial velocity will be the absolute value of either the sum or the difference of two terms. Note that the first term dominates the overall change of the radial velocity except for at the tangent point, where the second term dominates. The results are shown in Figure 1.

Although we only derived the projected velocity change for a case of an edge-on circular orbit, the same maximum velocity change is also valid when we include orbit inclinations. Because the radius of an actual orbit must be bigger than the observed projected distance, the projected radial velocity of an inclined orbit must be smaller than that of an edge-on orbit when other orbital parameters stay the same. If we consider cases of a constant inclination angle (θ), we will have similar formula. The only difference will be a cosine factor ($\cos\theta$) in the velocity terms. Therefore, we will have a new curve which is under the curve of the edge-on case, although the peak of the new curve will be at different positions for different inclination angles.
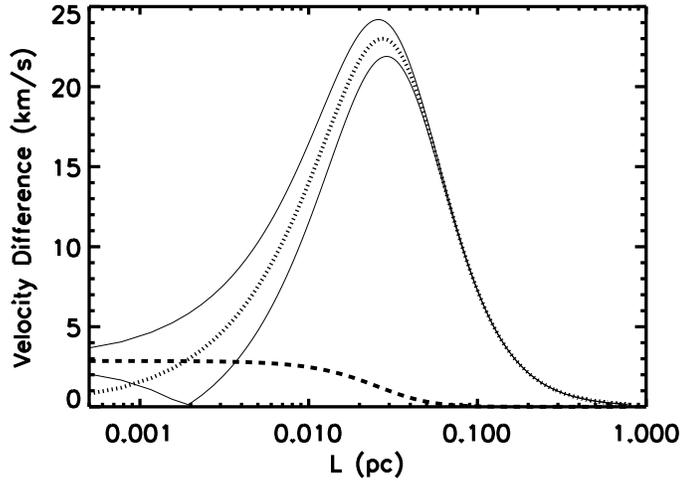

Fig. 1.— Absolute stellar radial velocity change, over a period of 5.8 years, as a function of the star's line-of-sight distance (L) from the tangent point of an edge-on circular orbit around the galactic center. Values are calculated using Eq. A6. Absolute values of two terms in the equation are shown with the dashed and dotted lines, respectively. The absolute values of the sum and difference of the two terms are shown with solid lines. The mass of the central black hole is assumed to be $3.5 \times 10^6 M_\odot$ and the radius of the orbit (R_0) is 1 arcsec at the distance of 8 kpc. Note that the value of the first term reaches its maximum when $L^2 = \frac{1}{2} R_0^2$.

REFERENCES

Alexander, T. 1999, ApJ, 527, 835

Alexander, T. & Livio, M. 2001, ApJ, 560, L143

Alexander, T. & Morris, M. 2003, ApJ, 590, L25

Allen, D. A., Hyland, A. R., & Hillier, D. J. 1990, MNRAS, 244, 706

Bahcall, J. N. & Tremaine, S. 1981, ApJ, 244, 805

Bahcall, J. N. & Wolf, R. A. 1976, ApJ, 209, 214

Bailey, V. C. & Davies, M. B. 1999, MNRAS, 308, 257

Binney, J. & Tremaine, S. 1987, Galactic dynamics (Princeton, NJ, Princeton University Press, 1987, 747 p.)

Blum, R. D., Sellgren, K., & Depoy, D. L. 1995, ApJ, 440, L17

—. 1996a, ApJ, 470, 864

—. 1996b, AJ, 112, 1988

D'Agostino, R. B., Belanger, A., & D'Agostino, Jr., R. B. 1990, The American Statistician, 44, 316

Davidge, T. J., Simons, D. A., Rigaut, F., Doyon, R., & Crampton, D. 1997, AJ, 114, 2586

Dehnen, W. & Binney, J. J. 1998, MNRAS, 298, 387

Eckart, A. & Genzel, R. 1997, MNRAS, 284, 576

Figer, D. F., Gilmore, D., Kim, S. S., Morris, M., Becklin, E. E., McLean, I. S., Gilbert, A. M., Graham, J. R., Larkin, J. E., Levenson, N. A., & Teplitz, H. I. 2003, ApJ, 599, 1139

Figer, D. F., McLean, I. S., & Najarro, F. 1997, ApJ, 486, 420

Genzel, R., Pichon, C., Eckart, A., Gerhard, O. E., & Ott, T. 2000, MNRAS, 317, 348

Genzel, R., Schödel, R., Ott, T., Eisenhauer, F., Hofmann, R., Lehnert, M., Eckart, A., Alexander, T., Sternberg, A., Lenzen, R., Clénet, Y., Lacombe, F., Rouan, D., Renzini, A., & Tacconi-Garman, L. E. 2003, ApJ, 594, 812

Genzel, R., Thatte, N., Krabbe, A., Kroker, H., & Tacconi-Garman, L. E. 1996, ApJ, 472, 153

Gerhard, O. 2001, ApJ, 546, L39

Ghez, A. M., Duchêne, G., Matthews, K., Hornstein, S. D., Tanner, A., Larkin, J., Morris, M., Becklin, E. E., Salim, S., Kremenek, T., Thompson, D., Soifer, B. T., Neugebauer, G., & McLean, I. 2003, ApJ, 586, L127

Ghez, A. M., Morris, M., Becklin, E. E., Tanner, A., & Kremenek, T. 2000, Nature, 407, 349

Ghez, A. M., Salim, S., Hornstein, S. D., Tanner, A., Lu, J. R., Morris, M., Becklin, E. E., & Duchêne, G. 2005, ApJ, 620, 744

Haller, J. W., Rieke, M. J., Rieke, G. H., Tamblyn, P., Close, L., & Melia, F. 1996, ApJ, 456, 194

Hanson, M. M. & Conti, P. S. 1994, ApJ, 423, L139+

Hanson, M. M., Conti, P. S., & Rieke, M. J. 1996, ApJS, 107, 281

Heisler, J., Tremaine, S., & Bahcall, J. N. 1985, ApJ, 298, 8

Krabbe, A., Genzel, R., Drapatz, S., & Rotaciuc, V. 1991, ApJ, 382, L19

Krabbe, A., Genzel, R., Eckart, A., Najarro, F., Lutz, D., Cameron, M., Kroker, H., Tacconi-Garman, L. E., Thatte, N., Weitzel, L., Drapatz, S., Geballe, T., Sternberg, A., & Kudritzki, R. 1995, ApJ, 447, L95+

Lacy, J. H., Townes, C. H., & Hollenbach, D. J. 1982, ApJ, 262, 120

Levin, Y. & Beloborodov, A. M. 2003, ApJ, 590, L33

Limber, D. N. & Mathews, W. G. 1960, ApJ, 132, 286

Lu, J. R., Ghez, A. M., Hornstein, S. D., Morris, M. R., Becklin, E. E., & Matthews, K. 2007, in American Astronomical Society Meeting Abstracts, Vol. 211, American Astronomical Society Meeting Abstracts, 33.05–+

Maillard, J. P., Paumard, T., Stolovy, S. R., & Rigaut, F. 2004, A&A, 423, 155

Martins. 2007, Personal communications

Martins, F., Genzel, R., Hillier, D. J., Eisenhauer, F., Paumard, T., Gillessen, S., Ott, T., & Trippe, S. 2007, ArXiv Astrophysics e-prints

Martins, F., Trippe, S., Paumard, T., Ott, T., Genzel, R., Rauw, G., Eisenhauer, F., Gillessen, S., Maness, H., & Abuter, R. 2006, ApJ, 649, L103

Merritt, D. 1987, ApJ, 313, 121

Merritt, D. & Szell, A. 2006, ApJ, 648, 890

Miralda-Escudé, J. & Gould, A. 2000, ApJ, 545, 847

Morris, M. 1993, ApJ, 408, 496

Morris, P. W., Eenens, P. R. J., Hanson, M. M., Conti, P. S., & Blum, R. D. 1996, ApJ, 470, 597

Najarro, F. 2007, Personal communications

Najarro, F., Hillier, D. J., Kudritzki, R. P., Krabbe, A., Genzel, R., Lutz, D., Drapatz, S., & Geballe, T. R. 1994, A&A, 285, 573

Najarro, F., Krabbe, A., Genzel, R., Lutz, D., Kudritzki, R. P., & Hillier, D. J. 1997, A&A, 325, 700

Ott, T., Eckart, A., & Genzel, R. 1999, ApJ, 523, 248

Ott, T., Genzel, R., Eckart, A., & Schödel, R. 2003, Astronomische Nachrichten Supplement, 324, 543

Paumard, T., Genzel, R., Martins, F., Nayakshin, S., Beloborodov, A. M., Levin, Y., Trippe, S., Eisenhauer, F., Ott, T., Gillessen, S., Abuter, R., Cuadra, J., Alexander, T., & Sternberg, A. 2006, ApJ, 643, 1011

Paumard, T., Maillard, J.-P., & Morris, M. 2004, A&A, 426, 81

Paumard, T., Maillard, J. P., Morris, M., & Rigaut, F. 2001, A&A, 366, 466

Paumard, T., Maillard, J.-P., & Stolovy, S. 2003, Astronomische Nachrichten Supplement, 324, 303

Peeples, M. S., Bonanos, A. Z., DePoy, D. L., Stanek, K. Z., Pepper, J., Pogge, R. W., Pinsonneault, M. H., & Sellgren, K. 2007, ApJ, 654, L61

Portegies Zwart, S. F., McMillan, S. L. W., & Gerhard, O. 2003, ApJ, 593, 352

Ramirez, S. V., Depoy, D. L., Frogel, J. A., Sellgren, K., & Blum, R. D. 1997, AJ, 113, 1411

Reid, M. J., Menten, K. M., Trippe, S., Ott, T., & Genzel, R. 2007, ApJ, 659, 378

Schödel, R., Eckart, A., Iserlohe, C., Genzel, R., & Ott, T. 2005, ApJ, 625, L111

Schödel, R., Ott, T., Genzel, R., Hofmann, R., Lehnert, M., Eckart, A., Mouawad, N., Alexander, T., Reid, M. J., Lenzen, R., Hartung, M., Lacombe, F., Rouan, D., Gendron, E., Rousset, G., Lagrange, A.-M., Brandner, W., Ageorges, N., Lidman, C., Moorwood, A. F. M., Spyromilio, J., Hubin, N., & Menten, K. M. 2002, Nature, 419, 694

Schödel, R., Eckart, A., Alexander, T., Merritt, D., Genzel, R., Sternberg, A., Meyer, L., Kul, F., Moultaka, J., Ott, T., & Straubmeier, C. 2007, A&A, 469, 125

Sellgren, K., McGinn, M. T., Becklin, E. E., & Hall, D. N. 1990, ApJ, 359, 112

Serabyn, E. & Lacy, J. H. 1985, ApJ, 293, 445

Tamblyn, P., Rieke, G. H., Hanson, M. M., Close, L. M., McCarthy, Jr., D. W., & Rieke, M. J. 1996, ApJ, 456, 206

Tanner, A., Figer, D. F., Najarro, F., Kudritzki, R. P., Gilmore, D., Morris, M., Becklin, E. E., McLean, I. S., Gilbert, A. M., Graham, J. R., Larkin, J. E., Levenson, N. A., & Teplitz, H. I. 2006, ApJ, 641, 891

Trippe, S., Martins, F., Ott, T., Paumard, T., Abuter, R., Eisenhauer, F., Gillessen, S., Genzel, R., Eckart, A., & Schödel, R. 2006, A&A, 448, 305

van der Marel, R. P. 1994, ApJ, 432, L91
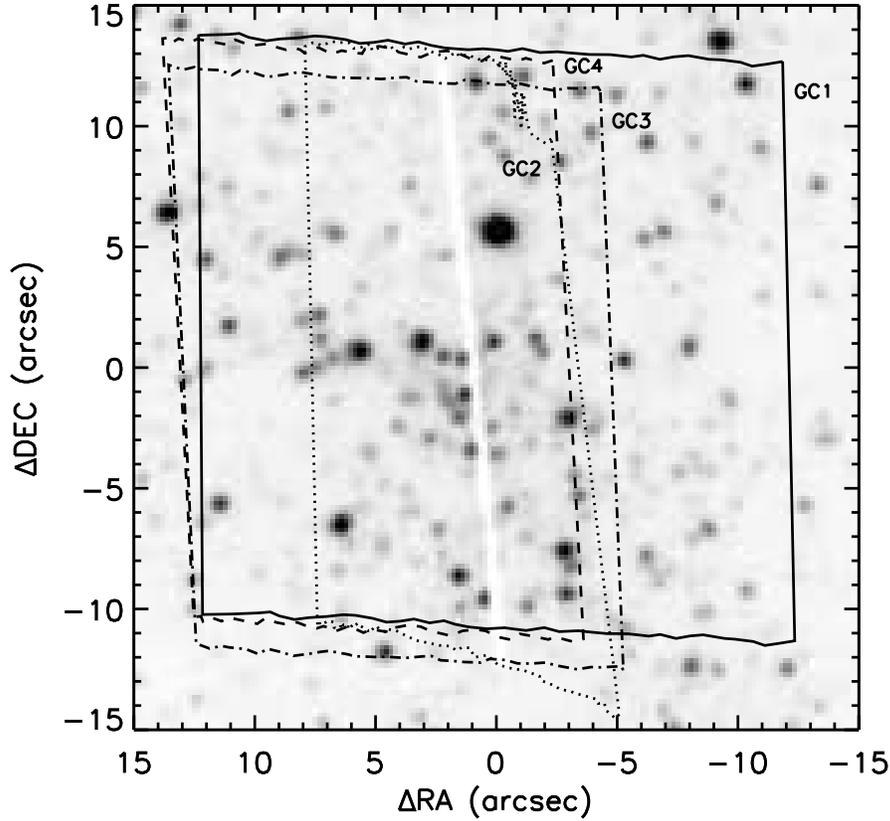
Fig. 2.— The slit-viewing camera image with boxes indicating sky areas covered by observations. Different types of lines are used to plot the boxes to avoid confusion. Dates of the observations are indicated with names of the slit scans (GC1: June 4th 1999, GC2: July 4th 1999, GC3: April 13th 2005, GC4: April 14th 2005). The nearly vertical white stripe at the middle of the image is the shadow of the slit which is cut through the mirror. The boundaries of boxes are computed based on slit position parameters.
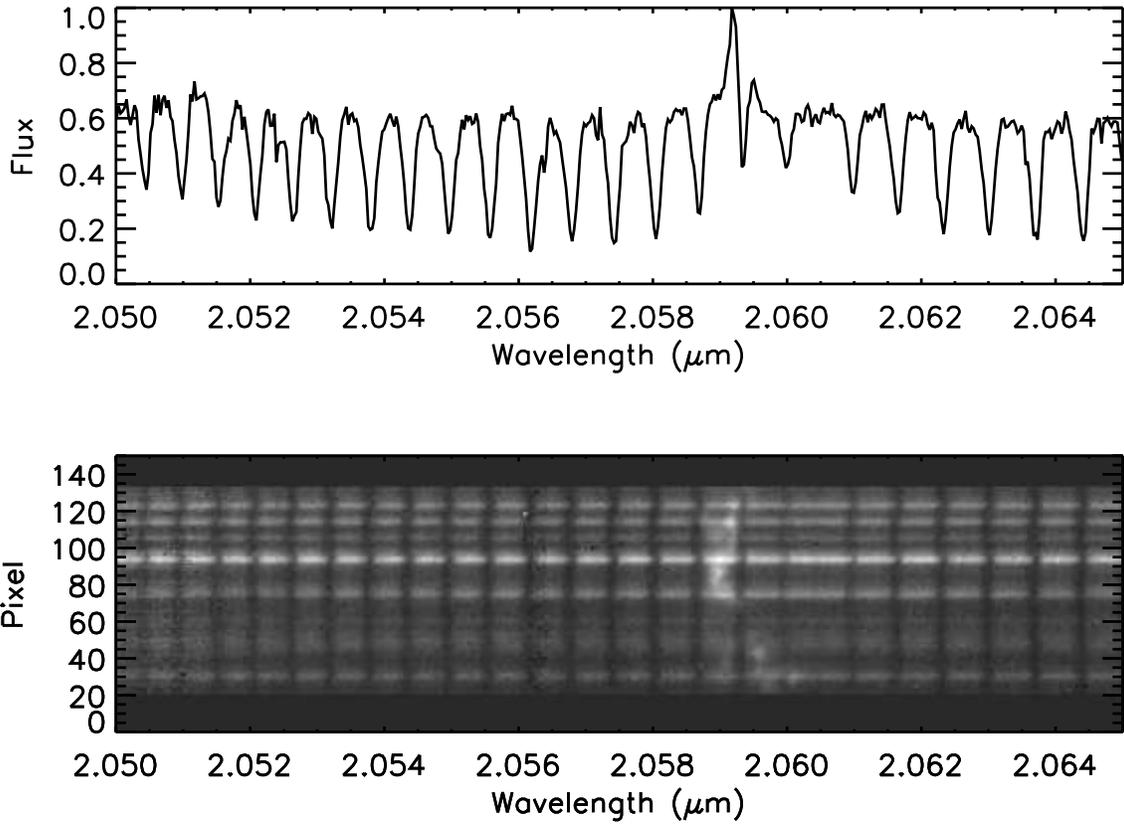
Fig. 3.— Telluric feature used to find spectral shifts caused by star position in slit and an example of rectified orders. Note the ripples, caused by star offset position in the slit, in atmospheric CO_2 absorption features (vertical dark lines in the image). Bright emission at ~2.06 μm is He I 2.0581 μm line emission from ISM. Image has been flipped so north is up.
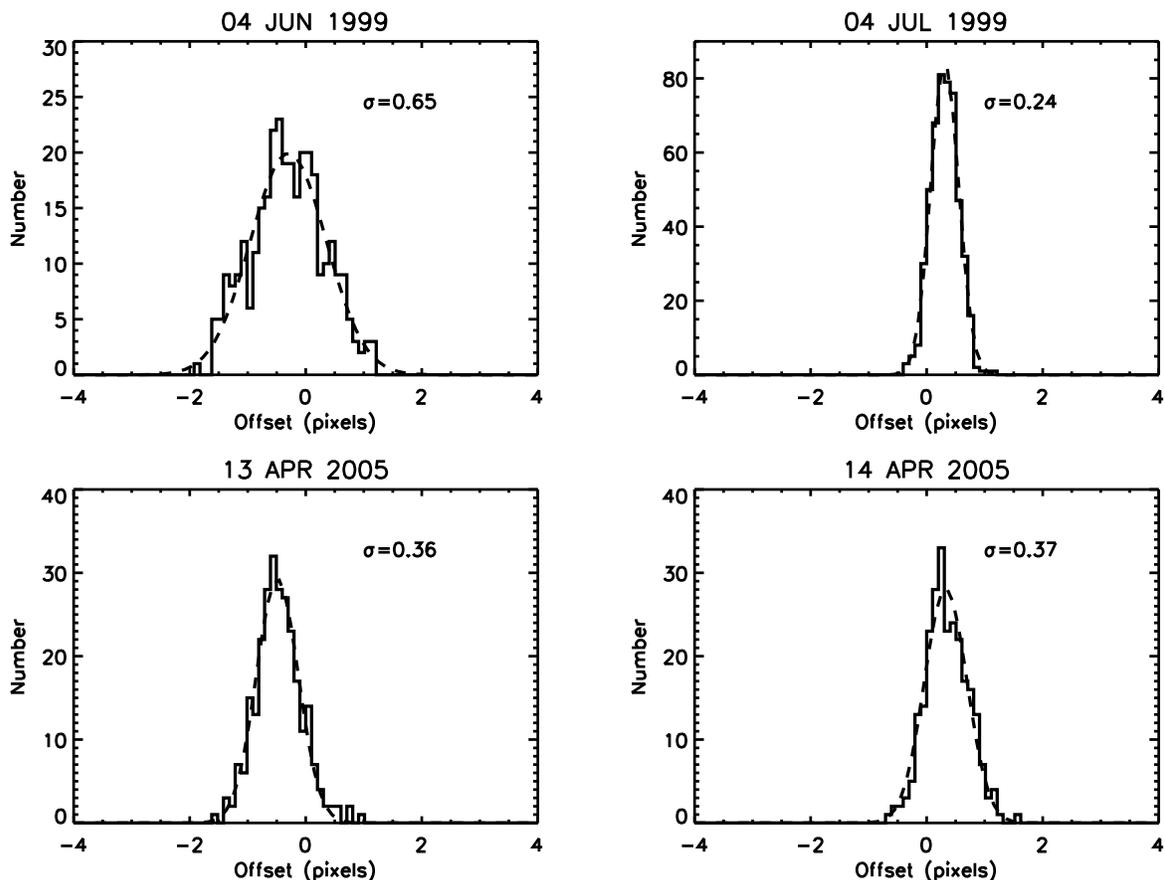
Fig. 4.— Distributions of star positions within slits. Stars are generally offset from the center of the slit. In order to correct for the spectral shift caused by this effect, the offset is found by cross-correlating CO_2 features in the spectra of target stars and a reference star, which is usually IRS7. Since IRS7 may also be offset from the center of the slit, the distributions of the offset are not centered at 0 as shown by these plots. The width of the distribution is proportional to the width of the slit used for each scan. Widths of Gaussian fits to the distributions are indicated in the plots.
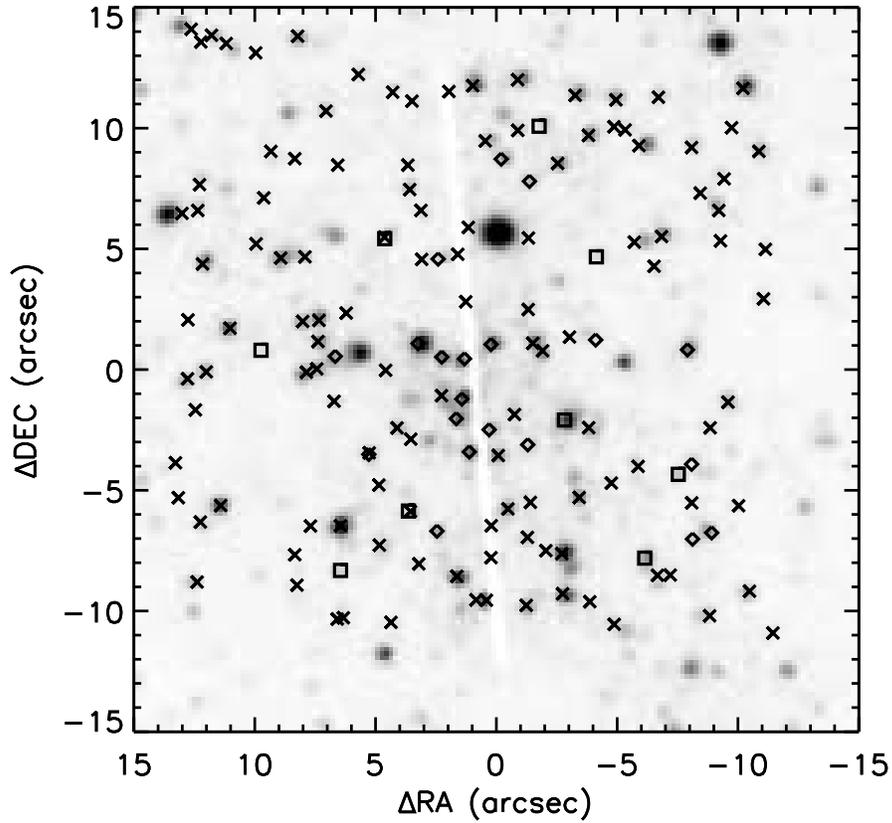
Fig. 5.— Positions of identified stars in four slit scans. The grey scale image shows the proximate sky area covered by four observations. The white strip in the middle of the field is the shadow of the slit. Cool stars are indicated with crosses, hot stars with He I 2.112/2.113μm doublet absorption feature are indicated with diamonds and hot stars showing He I 2.058μm broad emission are indicated with squares.
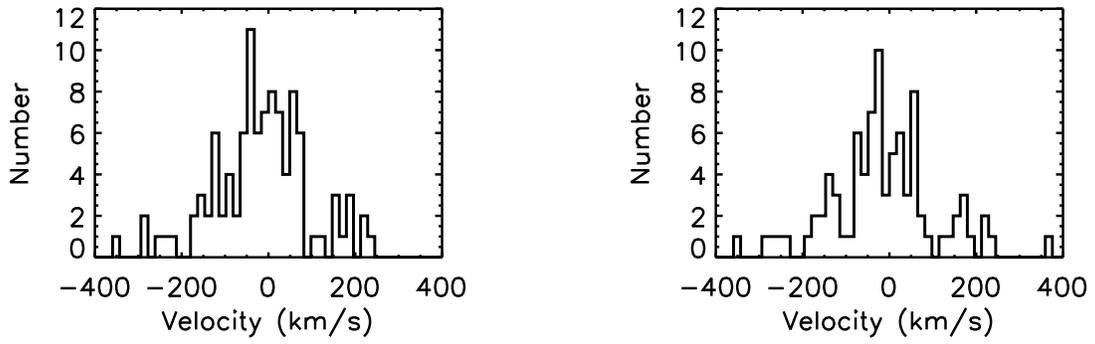
Fig. 6.— Distribution of radial velocities of cool stars in combined 1999 (left) and 2005 (right) data sets.
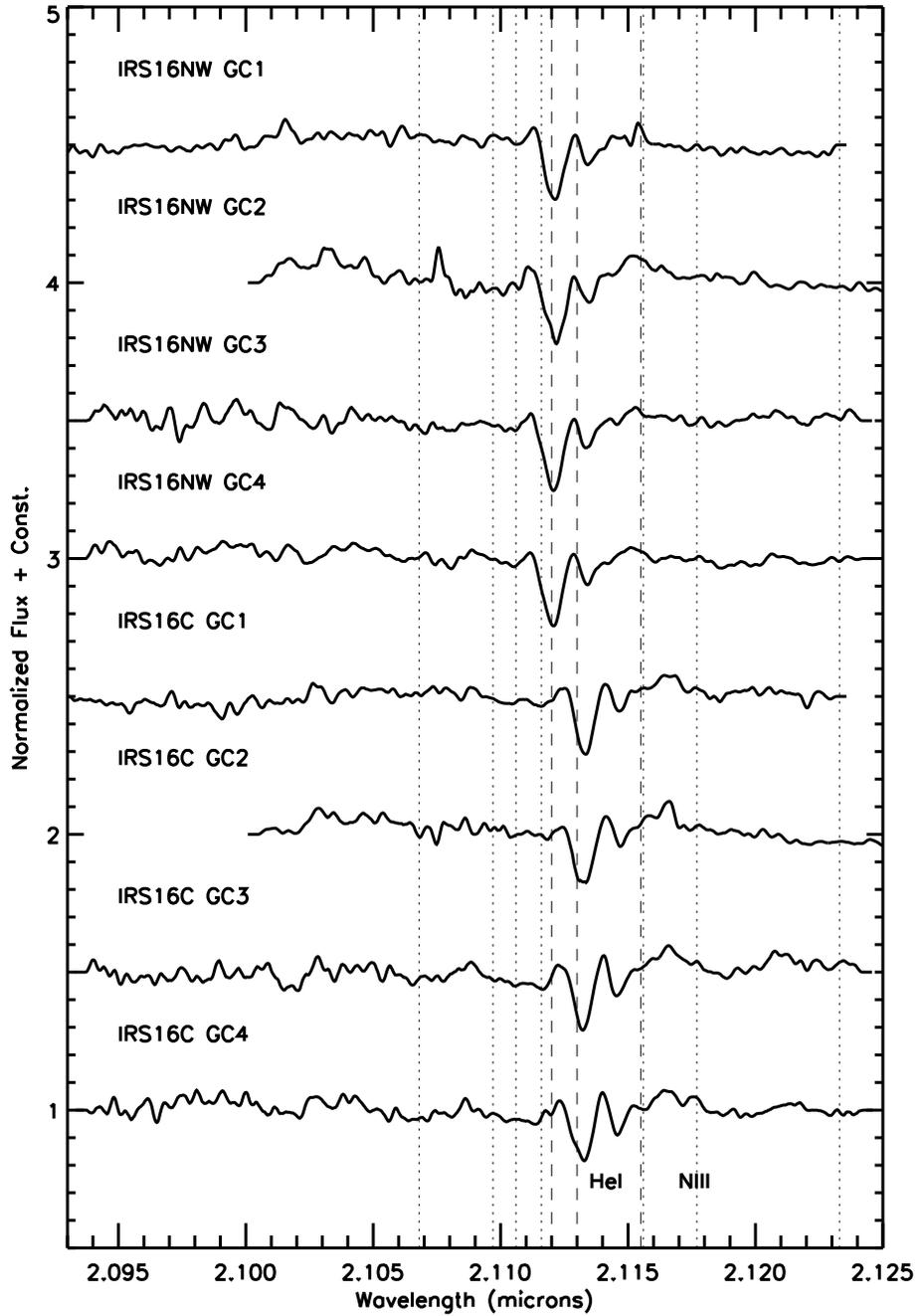
Fig. 7.— Spectra of He I stars showing the He I 2.112/2.113μm absorption doublet. Each spectrum is indicated with the name of the object followed by the name of the slit scan (GC1: June 4th 1999, GC2: July 4th 1999, GC3: April 13th 2005, GC4: April 14th 2005). Vertical dashed lines in the plots indicate the rest wavelengths of the photospherical lines and dotted lines indicate the rest wavelengths of telluric OH lines. The coadded spectra have been properly shifted to compensate the barycentric motions of the target star in each data set.
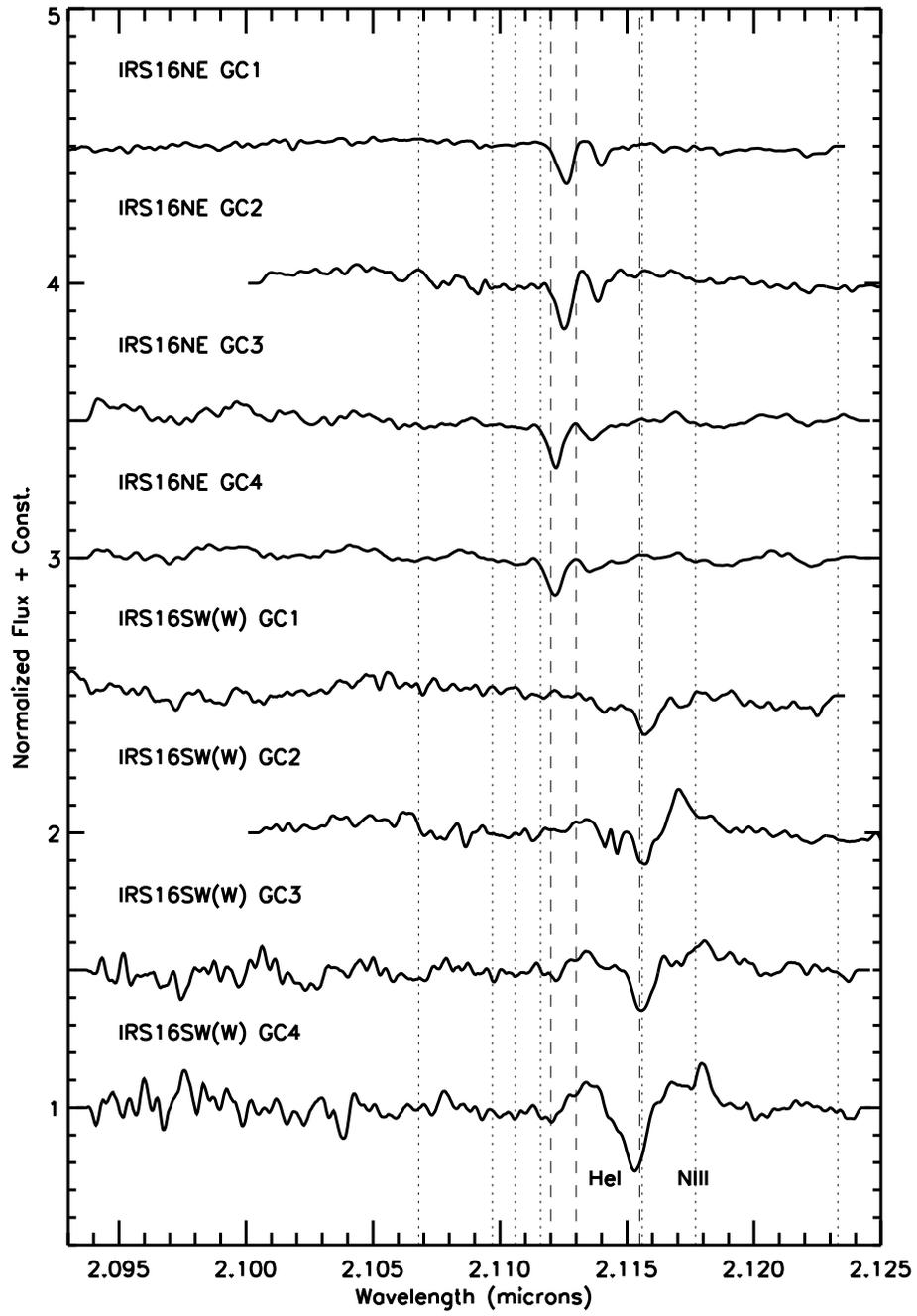
Fig. 7.— continued
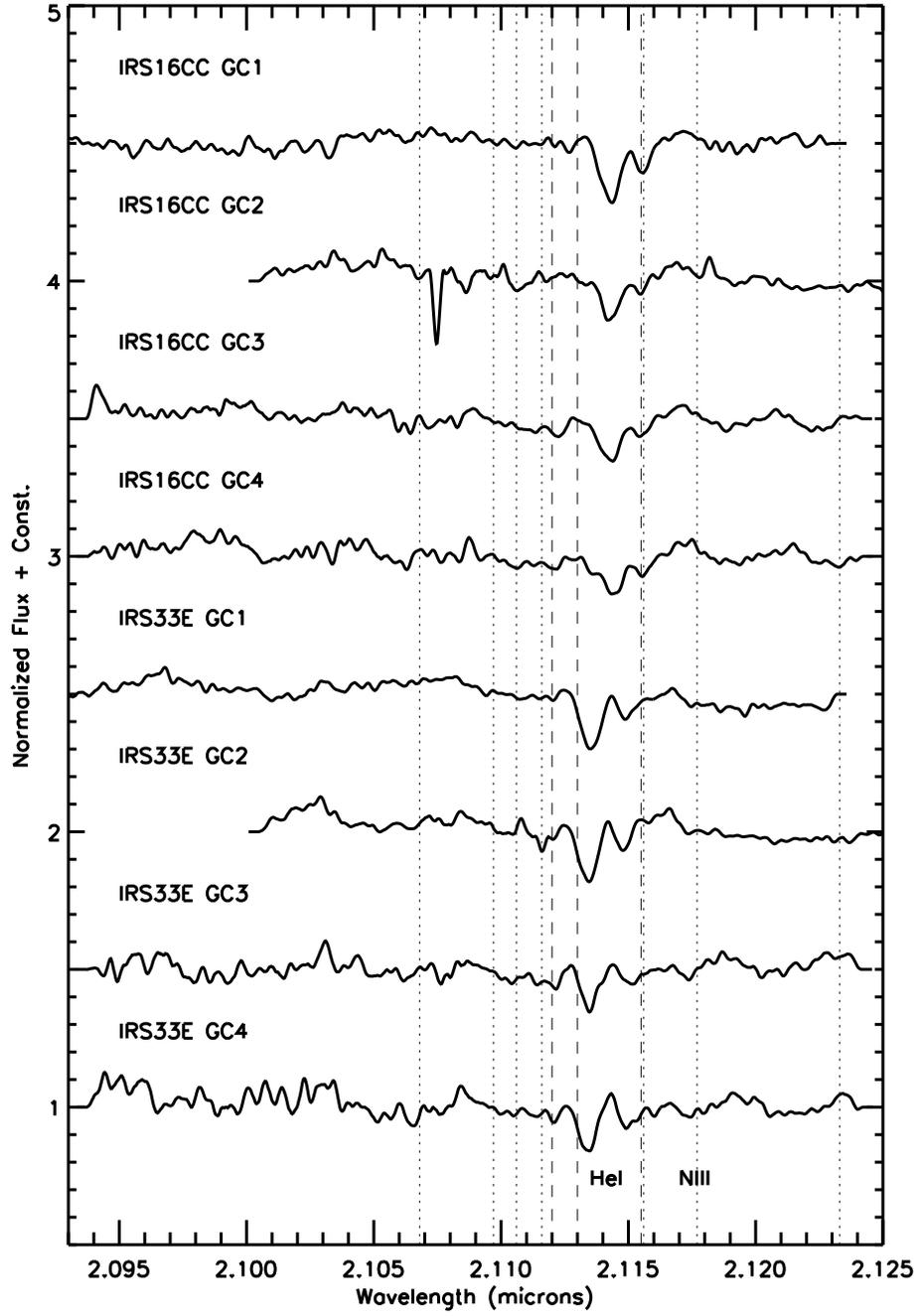
Fig. 7.— continued
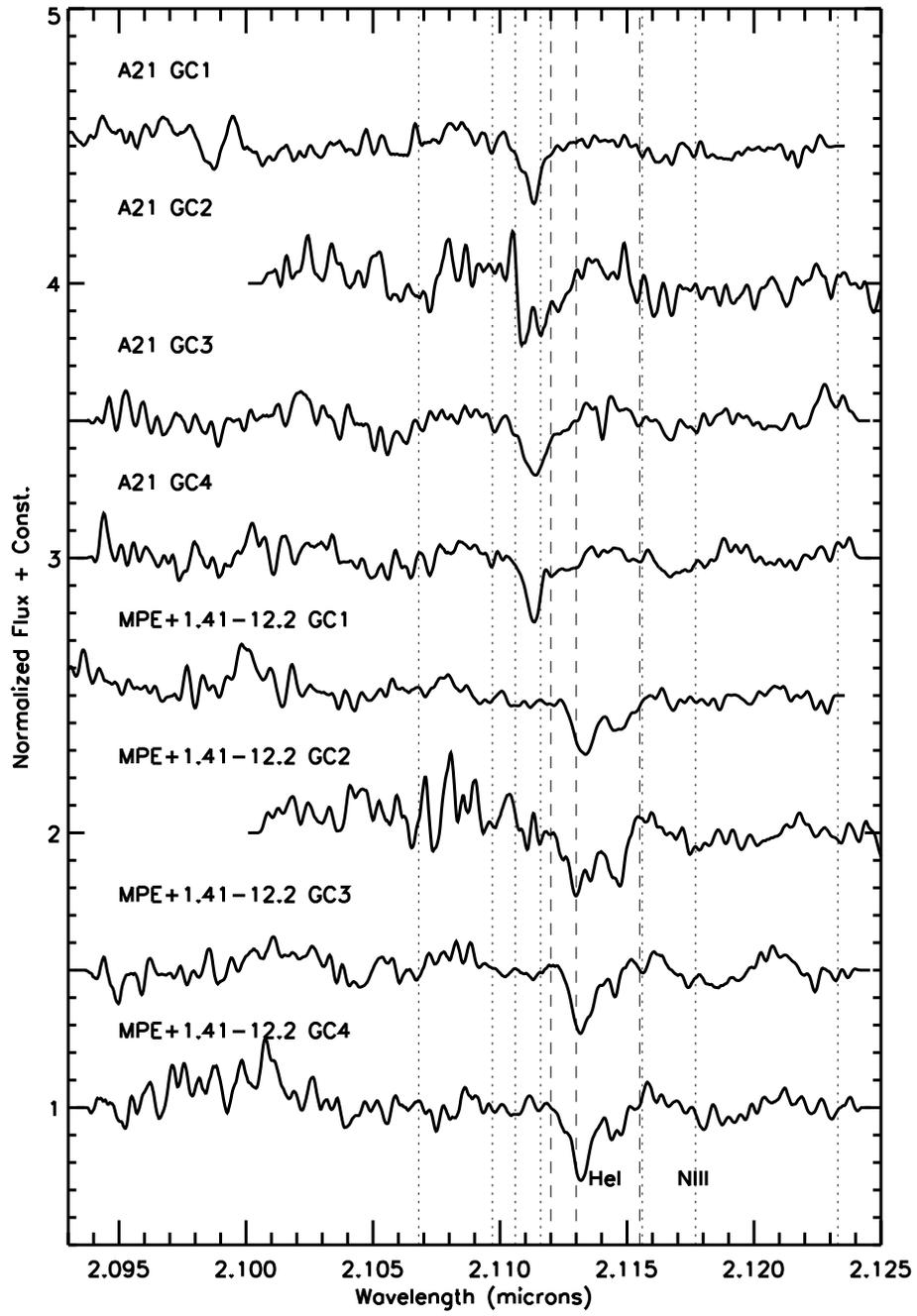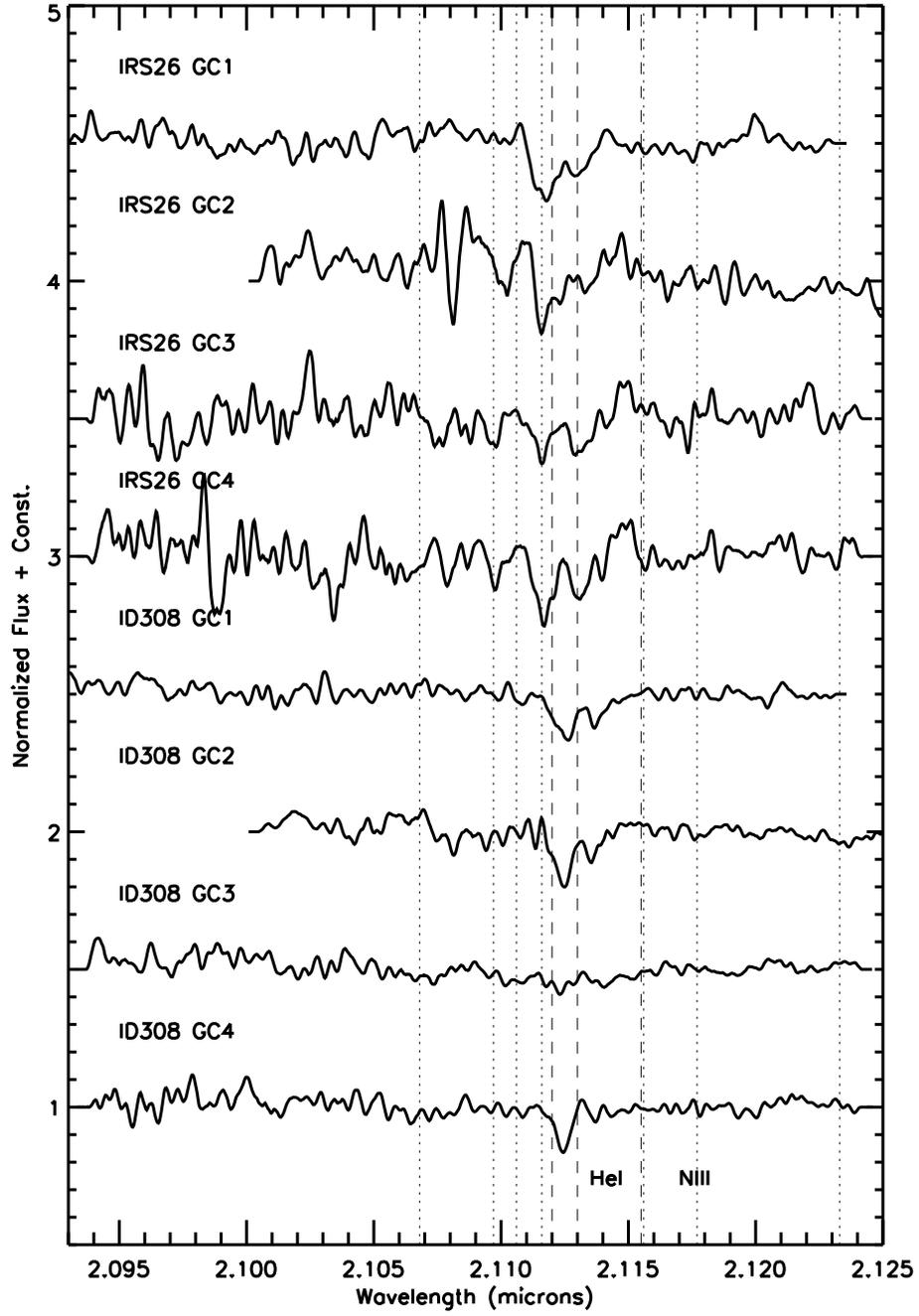
Fig. 7.— continued
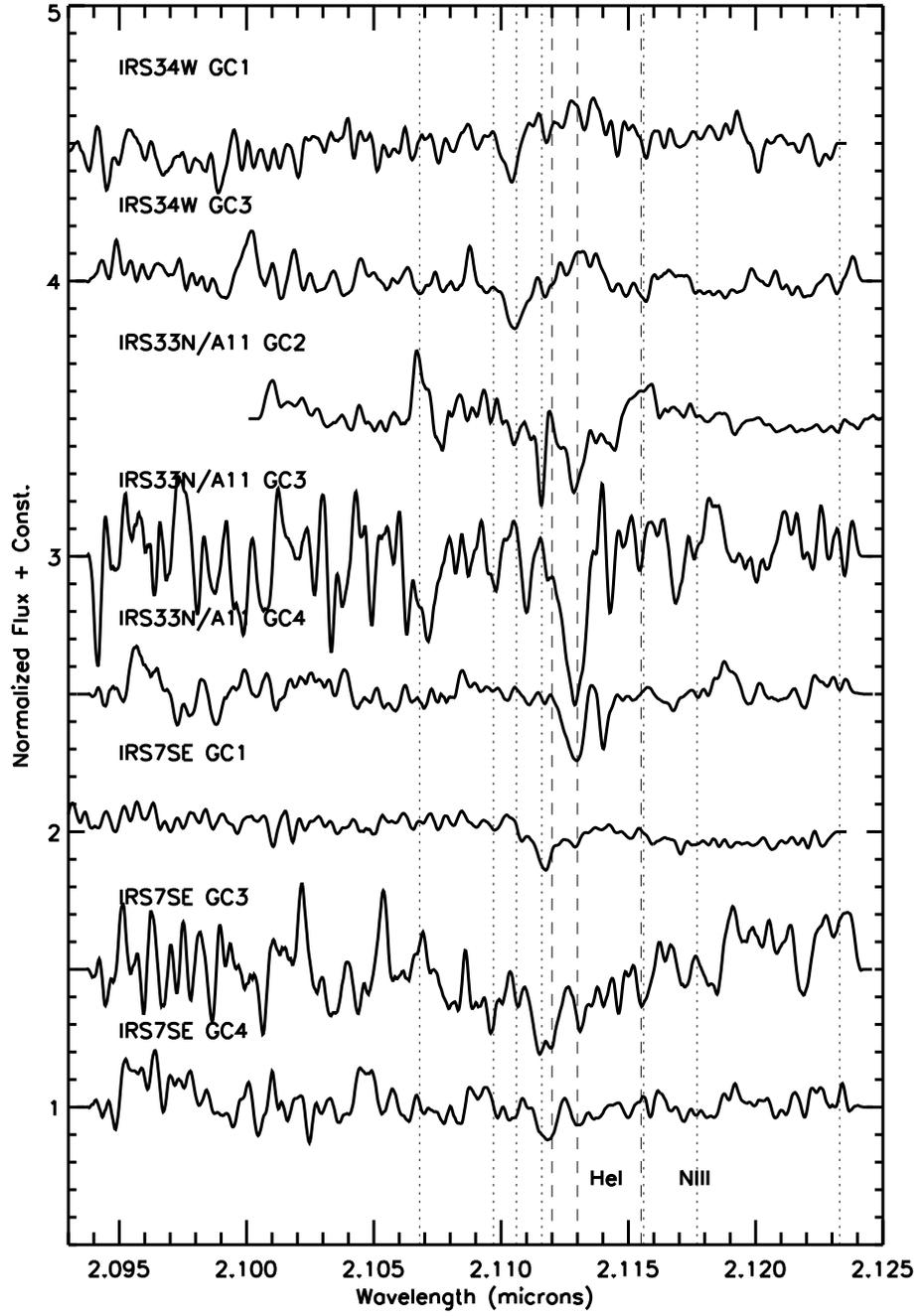
Fig. 7.— continued
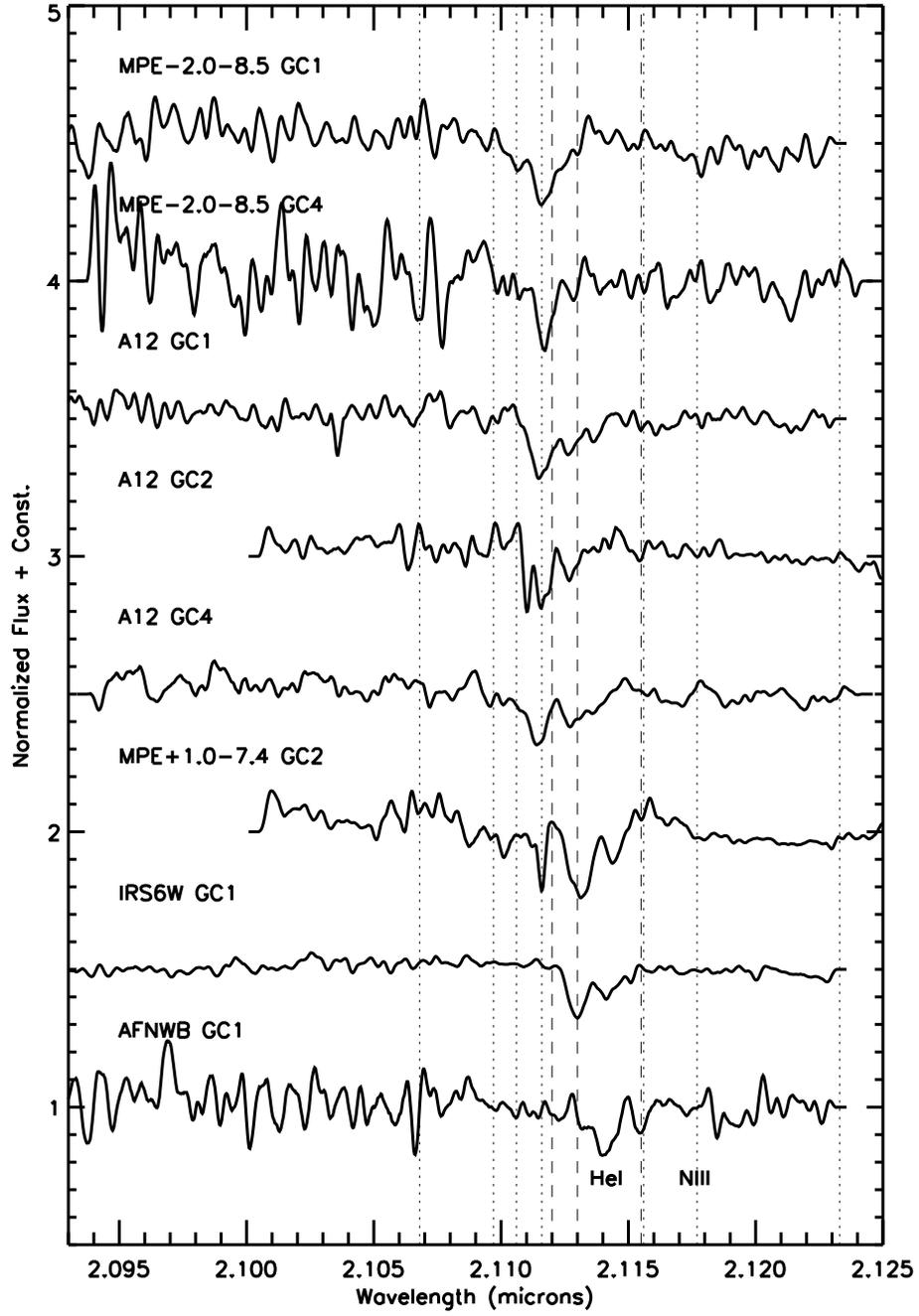
Fig. 7.— continued
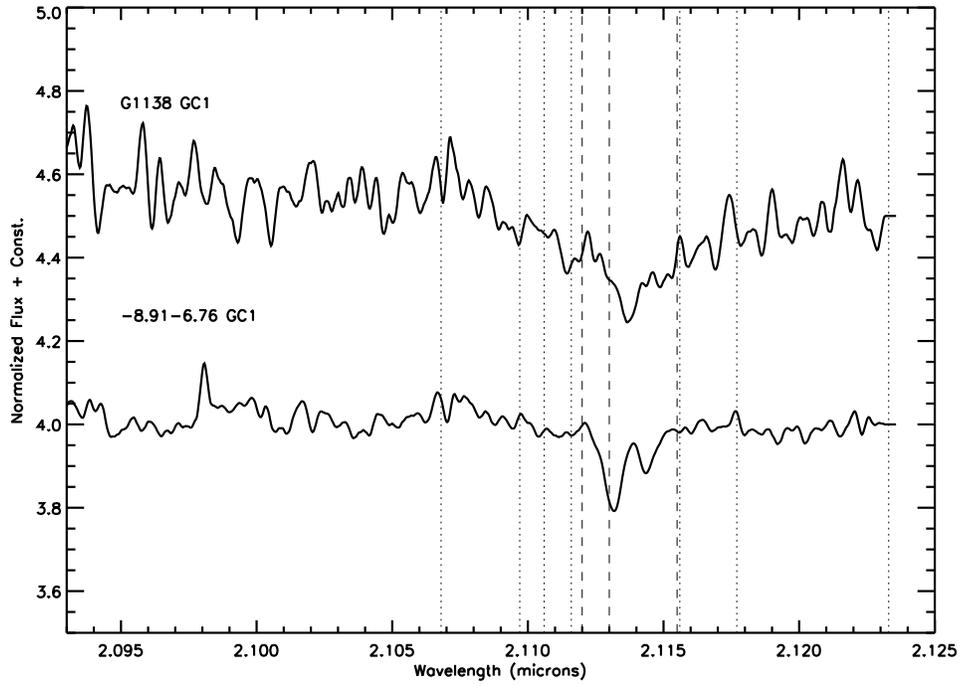
Fig. 7.— continued

Fig. 7.— continued
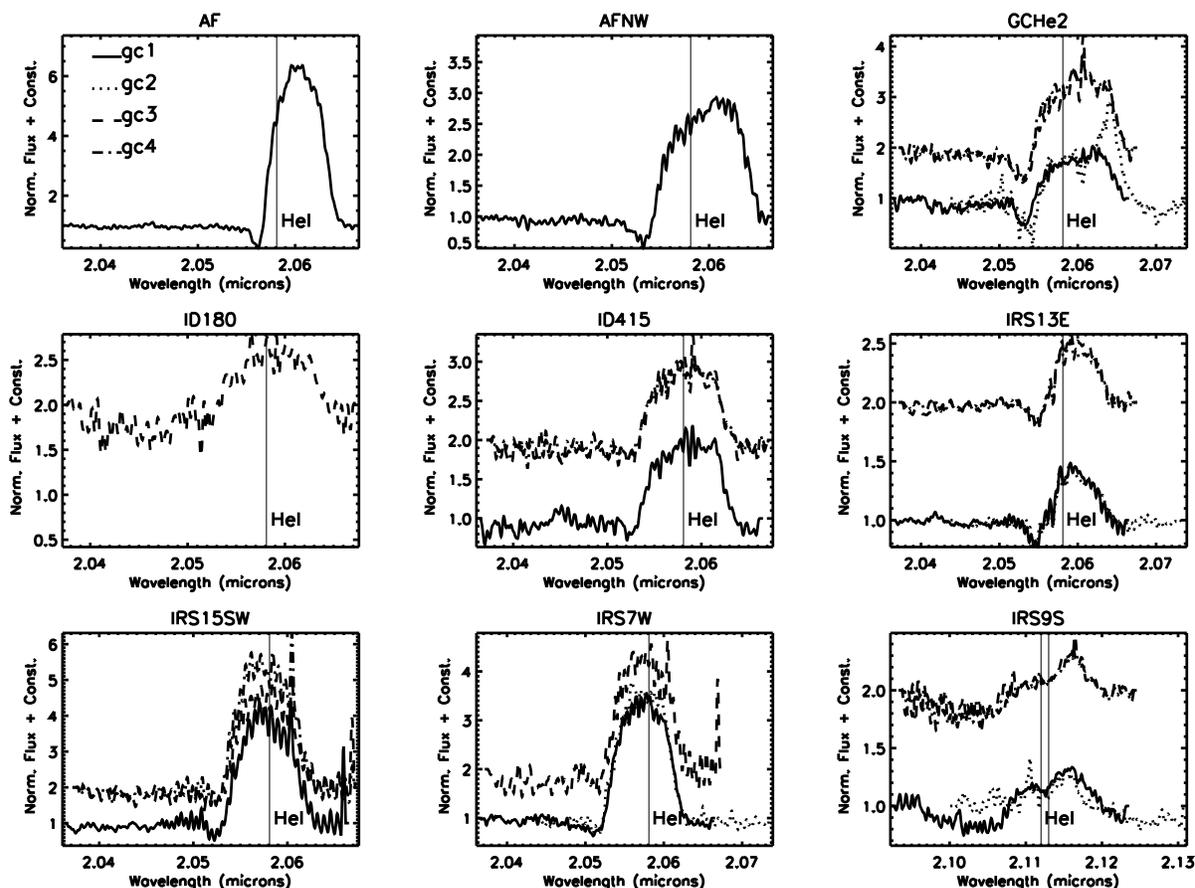
Fig. 8.— Spectra of He I stars showing the He I 2.058μm broad emission line. Spectra of different scans are plotted with different line types to avoid confusion. Spectra from two slit scans in 2005 are offset positively so that they are well separated from the spectra from two scans in 1999. The corresponding line styles are indicated by the names of slit scans at the upper left corner of the first panel. The vertical solid lines in the plots indicate the rest wavelengths of the He I lines. The coadded spectra have been properly shifted to compensate the barycentric motions of the target star in each data set. Strong repeating absorption features (zigzags) present in many spectra are the results of incomplete removal of telluric CO_2 lines (Figure 3). Imperfect background subtraction leaves residual nebula emission in some spectra, such as in that of GCHe2 from GC2.
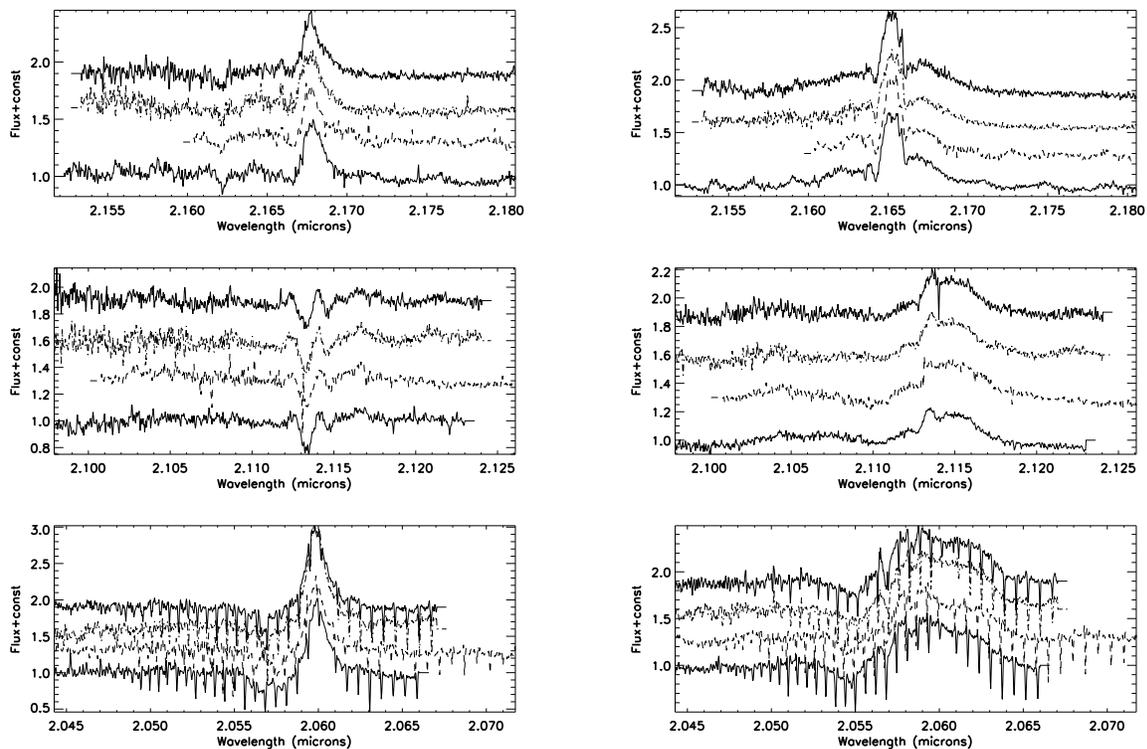
Fig. 9.— Examples of multiple night spectra of He I stars. Panels on the left are for IRS16C, a typical narrow line object. Panels on the right are for IRS13E, which is a broad line He I star. Three panels on each side show spectra centered at Brγ, He I 2.112 μm and He I 2.058 μm lines, respectively. In each panel, spectra from GC1, GC2, GC3 and GC4 are plotted from the bottom to the top. These figures demonstrate that the shapes of these lines do not change with time. Note that strong repeating absorption features seen in the spectra in the bottom panels are the results of incomplete removal of telluric CO2 lines.
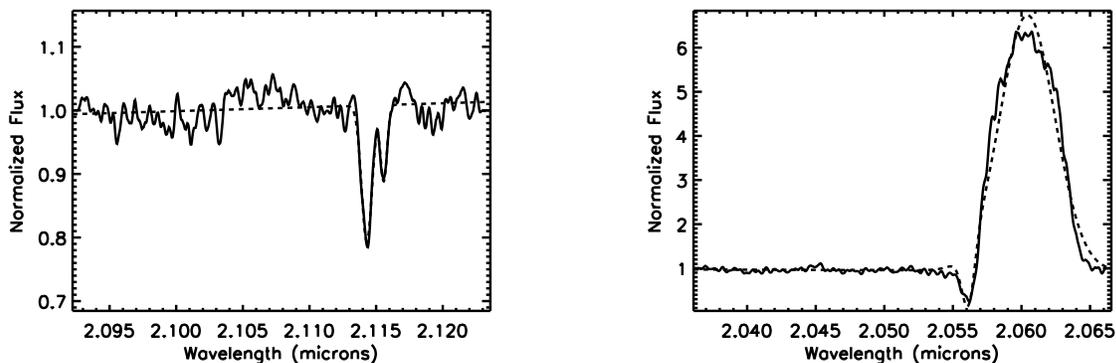
Fig. 10.— Examples of Gaussian fitting to the spectral lines of He I stars. The left panel shows an example of fitting the absorption doublet from a narrow-line object, IRS16CC. The right panel shows an example of fitting the P-Cygni profile emission line of a broad-line star, AF. Both spectra are acquired in GC1. In each plot, the continuum is fitted with a second degree polynomial.
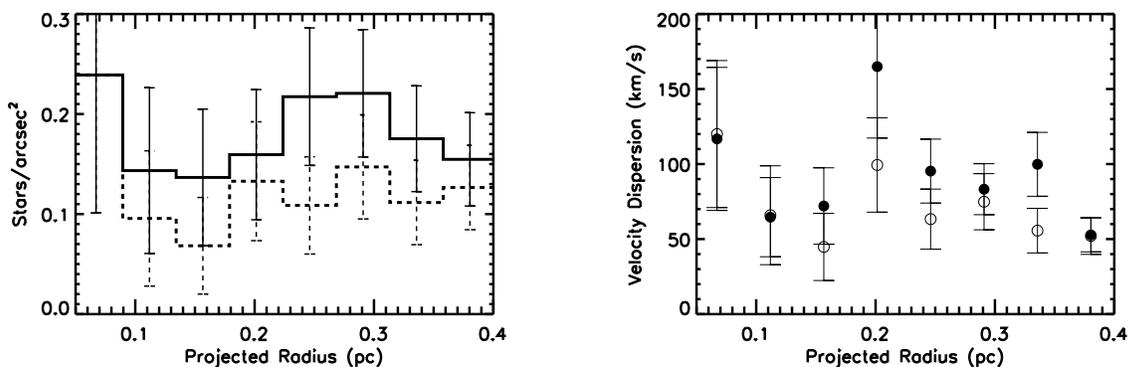
Fig. 11.— Surface number density (left) and radial velocity dispersion (right) of late type stars as functions of the projected distance from Sgr A*. Solid lines (filled circles) are for the current data and the dashed lines (open circles) are for the published data in Figer et al. (2003).
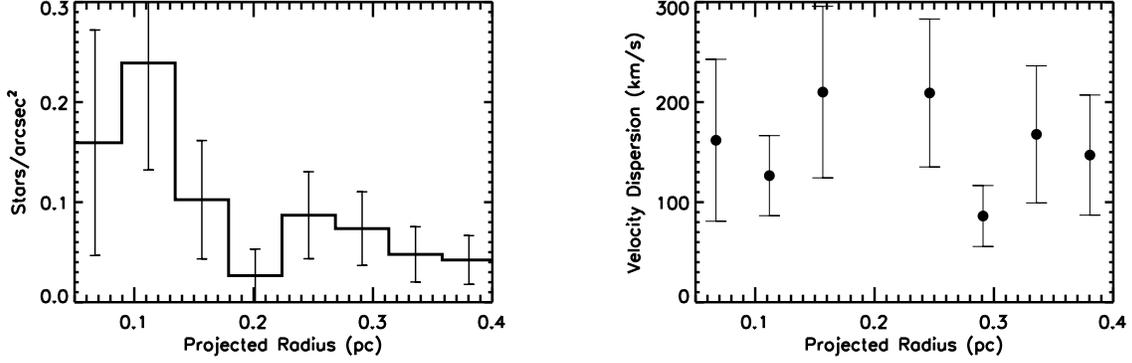
Fig. 12.— Surface number density (left) and radial velocity dispersion (right) of early type stars as functions of the projected distance from Sgr A*.
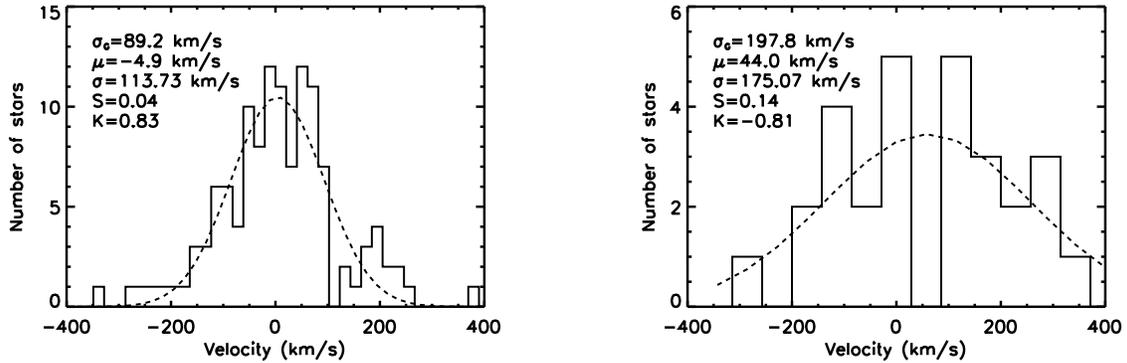
Fig. 13.— Distributions (histograms) and the best Gaussian fittings (dashed lines) of radial velocities of late type (left panel) and early type (right panel) stars. The standard deviations σ_G of the fitting functions are indicated. The statistical mean μ, the standard deviation σ, the skewness S and the excess kurtosis K of different samples are also shown. Note that a normal distribution should have a zero skewness and a zero kurtosis. The radial velocity measurements from different data sets for the same object are averaged before the computation of the distributions.
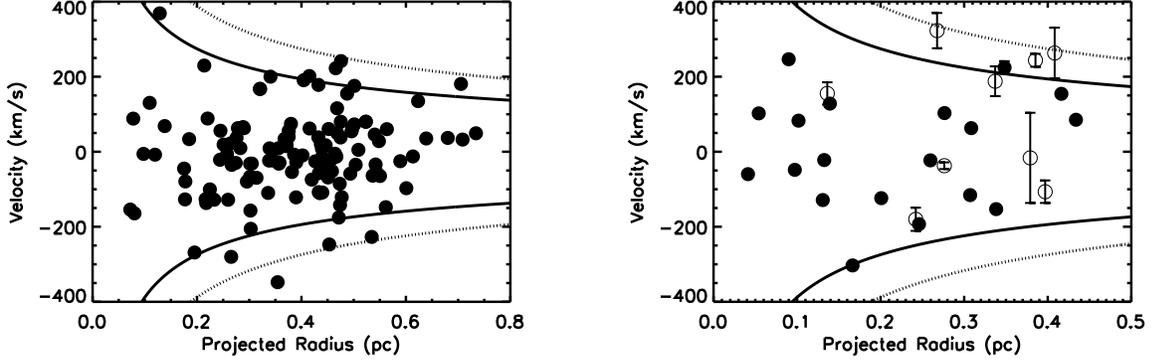
Fig. 14.— Radial velocities of stars as a function of projected Galactic radius. The left panel is for cool stars and the right panel is for hot stars. In the right panel, filled circles indicate stars showing narrow He I line absorption and open circles indicates stars showing broad He I line emission. Note that for some stars the size of the error bar is smaller than the symbol size. Solid curves in the figures show velocities for ideal circular orbits around a central mass of 3.5×10^6 M$_\odot$. Dashed curves show the escape velocities at the corresponding radii.
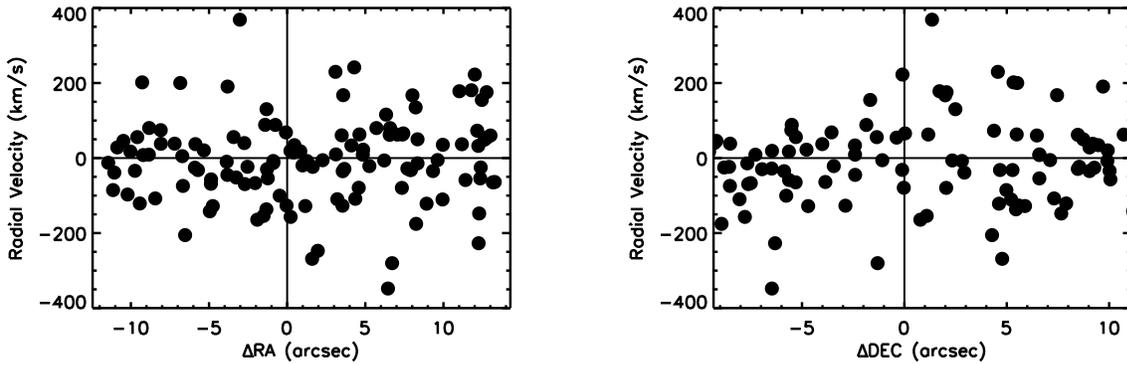
Fig. 15.— Radial velocities of cool stars vs. the RA and DEC offsets from Sgr A*. Note the sizes of error bars are smaller than the symbol size in these plots.
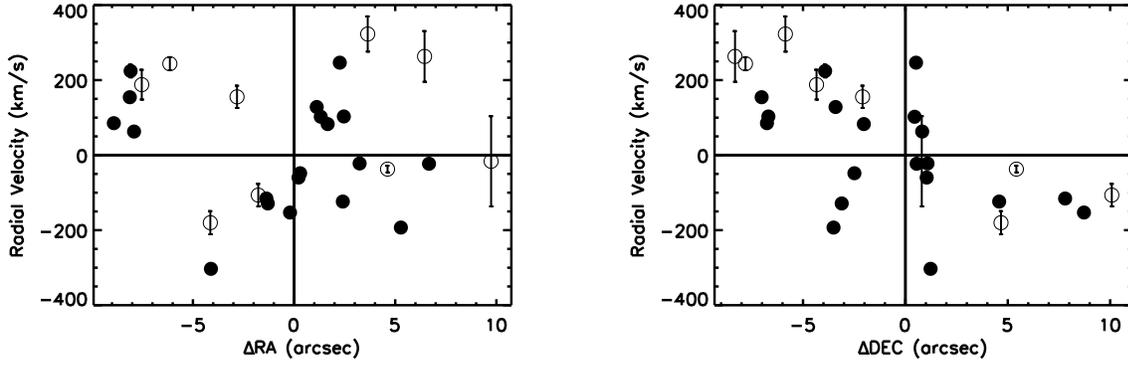
Fig. 16.— Radial velocities of hot stars vs. the RA and DEC offsets from Sgr A*. Narrow type stars are plotted with solid circles and broad type stars are plotted with open circles.
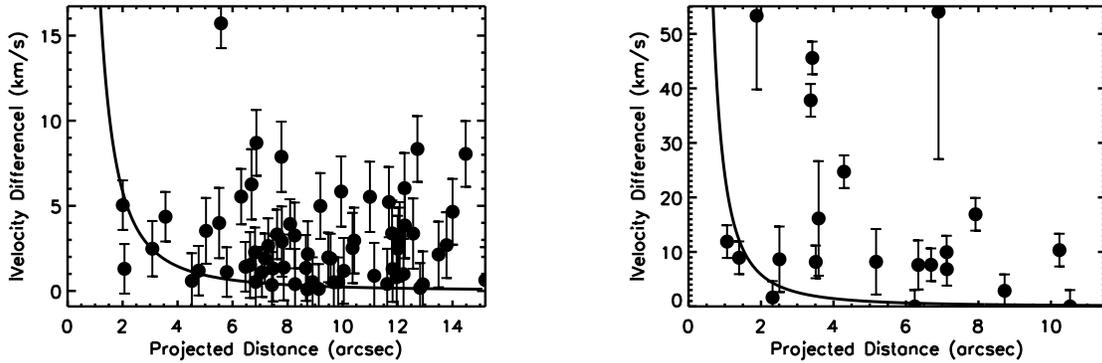
Fig. 17.— The difference of the radial velocities between 1999 and 2005 for cool stars (left panel) and hot stars (right panel) as a function of the projected Galactic radius. The solid curve shows the expected maximum radial velocity changes at different projected distances for an edge-on circular orbit system around a gravitationally dominant object with mass of 3.5×10^6 $M_\odot$.
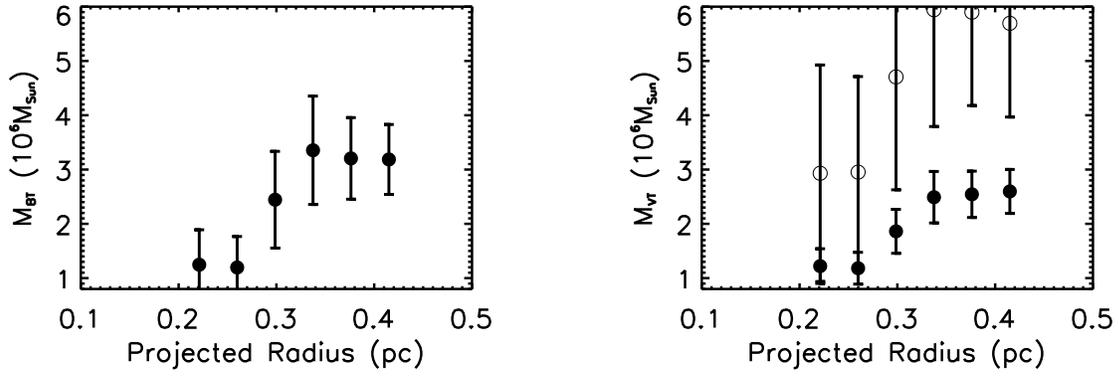
Fig. 18.— The estimated enclosed mass as a function of radius. The left panel shows the results from using the Bahcall-Tremaine estimator (Eq. 2) and the right panel shows the results using the Virial Theorem estimators (Eq. 3 and 4). The Bahcall-Tremaine estimator assumes the stellar velocities are isotropic and all mass is in a central point. The Virial Theorem estimators do not assume any anisotropy about the stellar velocities, but the assumption of all mass in a central point gives a lower limit (filled circles) and the assumption of mass following stars gives an upper limit (open circles) to the estimated black mass. Bigger error bars in the case of the Virial Theorem are due to the r_{ij}^{-1} term. In calculation, the maximum projected radius is set to keep the data set circularly symmetric about the GC. Both figures are based on the combined data set of observations in 1999 and 2005.

Table 1. Observational Parameters

Name[a]	Date	Resolution[b] $(R=\frac{\lambda}{\Delta\lambda})$	Filter[c]	IT (sec)	NFrame	Slit Size (arcsec×arcsec)
GC1	1999 JUN 04	14,000	NIRSPEC-7	60	40	0.72 × 24
GC2	1999 JUL 04	23,300	NIRSPEC-6/7	100	67	0.43 × 24
GC3	2005 APR 13	16,700	NIRSPEC-7	60	36	0.58 × 24
GC4	2005 APR 14	16,700	NIRSPEC-7	60	37	0.58 × 24

Note. — Parameters of individual observations. Integration time (IT) at each slit position and the total number of slit positions (NFrame) are shown in the table. The slit size is in units of arcsecs × arcsecs.

[a]Names referring different slit scans in the order of the dates when observations were carried out.

[b]The resolution is $\lambda/\Delta\lambda_{FWHM}$, where $\Delta\lambda_{FWHM}$ is the half-power line width of arc lamp lines. The values are measured at $\lambda = 2.171407$ μm. $\Delta\lambda \simeq 1.561\times10^{-4}$, 9.286×10^{-5}, 1.296×10^{-4} and 1.301×10^{-4} μm for GC1, GC2, GC3 and GC4 respectively. The slit width was 5 pixels in GC1, 3 pixels in GC2 and 4 pixels in GC3 and GC4.

[c]NIRSPEC-7 has half-power points of 1.85 and 2.62 μm. NIRSPEC-6 has half-power points of 1.56 and 2.30 μm. Half-power points are taken from Figer et al. (2003).

Table 2. Wavelength Ranges of Echelle Orders (μm)

Echelle Order	GC1 Min	GC1 Max	GC2 Min	GC2 Max	GC3 Min	GC3 Max	GC4 Min	GC4 Max
32	-	-	-	-	2.353	2.388	2.353	2.388
33	2.281	2.315	2.290	2.324	2.282	2.316	2.282	2.316
34	2.214	2.248	2.223	2.256	2.215	2.249	2.215	2.249
35	2.152	2.184	2.160	2.192	2.152	2.185	2.152	2.185
36	2.092	2.124	2.100	2.131	2.093	2.124	2.093	2.124
37	2.036	2.067	2.044	2.074	2.037	2.067	2.037	2.067

Note. — Wavelength Coverage of different data sets. Because the orders are longer than the width of the detector, the spectra are not contiguous in wavelength. The wavelengths are in microns.

Table 3.   Cool Star Velocity

Name	RA (″)	DEC (″)	V99 (km s^{-1})	V05 (km s^{-1})	V$_{avg}$ (km s^{-1})	Temp (K)	Spectral Type	V$_{Figer}$ (km s^{-1})
ID327	-1.51	1.09	-154.1 ± 1.8	...	-154.1 ± 1.8	5161	<G8III	-156.0 ± 1.1
ID259	-0.75	-1.86	85.8 ± 1.3	90.8 ± 0.7	88.3 ± 1.5	3714	M1III	96.5 ± 0.8
IRS29S	-1.91	0.78	-165.0 ± 1.3	-163.7 ± 0.7	-164.3 ± 1.5	4338	K2III	-160.0 ± 1.1
2.27-1.08	2.27	-1.08	-5.7 ± 1.8	...	-5.7 ± 1.8	4996	<G8III	...
G288?	-1.32	2.49	130.3 ± 1.3	...	130.3 ± 1.3	4167	K3III	133.7 ± 1.1
ID365	1.26	2.81	-6.6 ± 1.3	-9.1 ± 1.0	-7.8 ± 1.6	4206	K3III	1.9 ± 1.1
-3.03+1.35	-3.03	1.35	...	368.9 ± 1.0	368.9 ± 1.0	5004	<G8III	...
IRS33W	-0.08	-3.56	66.2 ± 1.3	70.6 ± 0.7	68.4 ± 1.5	3697	M2III	73.5 ± 0.8
IRS13W	-3.83	-2.40	-44.6 ± 1.3	-45.2 ± 1.0	-44.9 ± 1.6	3865	M0III	-40.0 ± 1.1
3.54-2.88	3.54	-2.88	-127.0 ± 1.8	...	-127.0 ± 1.8	4482	K1III	...
4.58-0.03	4.58	-0.03	-79.2 ± 1.8	...	-79.2 ± 1.8	4620	K0III	...
ID244	4.11	-2.41	33.0 ± 1.3	34.2 ± 0.7	33.6 ± 1.5	3628	M2III	40.3 ± 0.8
ID398	1.60	4.77	-270.4 ± 1.8	-266.9 ± 0.7	-268.6 ± 1.9	4194	K3III	-262.0 ± 1.1
3.09+4.56	3.09	4.56	231.8 ± 1.8	227.8 ± 1.0	229.8 ± 2.1	4430	K1III	...
IRS7	-0.04	5.58	-118.7 ± 1.3	-134.4 ± 0.7	-126.5 ± 1.5	3364	M7III	-109.0 ± 0.8
-1.33+5.45	-1.33	5.45	...	-136.7 ± 1.0	-136.7 ± 1.0	4380	K1III	...
-1.41-5.50	-1.41	-5.50	88.6 ± 1.8	...	88.6 ± 1.8	4310	K2III	...
IRS20	-0.48	-5.77	-99.8 ± 1.3	-100.9 ± 0.7	-100.4 ± 1.5	3246	>M7III	-90.9 ± 0.8
1.16+5.89	1.16	5.89	...	-127.9 ± 1.0	-127.9 ± 1.0	4316	K2III	...
5.26-3.45	5.26	-3.45	...	-21.4 ± 0.7	-21.4 ± 0.7	5123	<G8III	...
-3.43-5.30	-3.43	-5.30	53.2 ± 1.3	58.7 ± 1.0	56.0 ± 1.6	3492	M4III	...
G577A?	0.21	-6.47	18.5 ± 1.3	19.9 ± 0.7	19.2 ± 1.5	3687	M2III	28.5 ± 0.8
6.21+2.34	6.21	2.34	-5.6 ± 1.8	-7.1 ± 0.7	-6.4 ± 1.9	4053	K4III	...
-4.76-4.70	-4.76	-4.70	-124.9 ± 1.8	-131.1 ± 1.0	-128.0 ± 2.1	4106	K4III	...
ID189	4.86	-4.78	23.4 ± 1.3	21.2 ± 0.7	22.3 ± 1.5	4105	K4III	26.9 ± 1.1
6.71-1.31	6.72	-1.31	-280.0 ± 1.3	-280.5 ± 0.7	-280.2 ± 1.5	4364	K1III	...
GCHe2	3.56	-5.88	-39.4 ± 1.8	-30.7 ± 0.7	-35.0 ± 1.9	5033	<G8III	...
ID144	-1.29	-6.95	-30.3 ± 1.3	-29.2 ± 0.7	-29.8 ± 1.5	3610	M3III	-22.3 ± 0.8
ID213	-5.87	-4.01	37.2 ± 1.8	...	37.2 ± 1.8	4118	K3III	41.1 ± 1.1
ID415	4.63	5.48	62.0 ± 1.3	64.0 ± 0.7	63.0 ± 1.5	4271	K2III	68.2 ± 0.8
ID430	3.12	6.60	11.0 ± 1.3	8.4 ± 1.0	9.7 ± 1.6	3887	M0III	16.0 ± 1.1
ID297	7.43	0.03	65.8 ± 1.8	65.5 ± 0.7	65.7 ± 1.9	3873	M0III	71.1 ± 1.1
IRS1NE(3)	7.38	1.16	62.1 ± 1.8	63.4 ± 0.7	62.8 ± 1.9	3824	M0III	72.7 ± 1.1
IRS1NE(2)	7.34	2.04	-77.8 ± 1.3	-81.2 ± 0.7	-79.5 ± 1.5	3623	M3III	-68.8 ± 1.1
-2.05-7.50	-2.05	-7.50	...	-66.8 ± 1.0	-66.8 ± 1.0	3649	M2III	...
BHA4E	-5.71	5.28	-35.9 ± 1.8	-28.0 ± 1.0	-32.0 ± 2.1	3679	M2III	-28.2 ± 1.1
ID126	0.22	-7.79	-158.3 ± 1.8	-155.4 ± 1.0	-156.8 ± 2.1	4415	K1III	-146.0 ± 0.8
-6.53+4.28	-6.53	4.28	-205.4 ± 1.8	...	-205.4 ± 1.8	4208	K3III	...
7.86-0.11	7.86	-0.11	-30.9 ± 1.8	-32.2 ± 0.7	-31.5 ± 1.9	3562	M3III	...
IRS12N	-2.71	-7.63	-67.5 ± 1.3	-71.4 ± 0.7	-69.4 ± 1.5	3851	M0III	-60.7 ± 0.8
IRS1NE(1)	8.02	2.00	168.9 ± 1.8	165.6 ± 0.7	167.3 ± 1.9	3437	M5III	-67.5 ± 1.1
3.58+7.45	3.59	7.45	167.9 ± 1.8	167.4 ± 1.0	167.6 ± 2.1	4905	<G8III	...
G849?	3.21	-8.05	-110.4 ± 1.8	-109.1 ± 0.7	-109.8 ± 1.9	4073	K4III	-107.0 ± 1.1
IRS14N	1.63	-8.56	-23.5 ± 1.3	-23.5 ± 0.7	-23.5 ± 1.5	3313	>M7III	-13.6 ± 0.8
4.84-7.27	4.84	-7.27	10.1 ± 1.8	7.9 ± 0.7	9.0 ± 1.9	4283	K2III	...

Table 3—Continued

Name	RA (″)	DEC (″)	V99 (km s⁻¹)	V05 (km s⁻¹)	V$_{avg}$ (km s⁻¹)	Temp (K)	Spectral Type	V$_{Figer}$ (km s⁻¹)
BHA4W	-6.84	5.51	200.1 ± 1.8	...	200.1 ± 1.8	3346	M7III	...
ID467	-2.54	8.54	-23.0 ± 1.3	-23.5 ± 0.7	-23.2 ± 1.5	3394	M6III	-13.8 ± 0.8
IRS9	6.45	-6.47	-347.8 ± 1.3	-347.7 ± 0.7	-347.8 ± 1.5	4012	K4III	-341.0 ± 0.8
-8.85-2.41	-8.85	-2.41	9.1 ± 1.8	...	9.1 ± 1.8	3529	M4III	...
7.92+4.67	7.92	4.67	-29.3 ± 1.8	-34.3 ± 0.7	-31.8 ± 1.9	3765	M1III	...
3.66+8.47	3.66	8.47	-28.9 ± 1.8	...	-28.9 ± 1.8	4906	<G8III	...
G904	0.46	9.47	35.3 ± 1.3	33.4 ± 0.7	34.4 ± 1.5	3314	>M7III	43.8 ± 0.8
IRS14SW	0.41	-9.56	14.1 ± 1.3	15.9 ± 0.7	15.0 ± 1.5	3853	M0III	24.5 ± 0.8
0.84-9.54	0.84	-9.54	...	18.1 ± 1.0	18.1 ± 1.0	3235	>M7III	...
IRS12S	-2.74	-9.28	40.2 ± 1.3	39.7 ± 0.7	40.0 ± 1.5	3498	M4III	48.8 ± 0.8
G986	-9.59	-1.35	55.8 ± 1.8	...	55.8 ± 1.8	3747	M1III	62.7 ± 1.1
-8.09-5.52	-8.09	-5.52	74.4 ± 1.8	...	74.4 ± 1.8	4349	K2III	...
ID87	-1.24	-9.76	-54.2 ± 1.3	-53.7 ± 0.7	-54.0 ± 1.5	3874	M0III	-46.0 ± 0.8
ID498	-0.89	9.91	-4.9 ± 1.8	-10.7 ± 1.0	-7.8 ± 2.1	3761	M1III	-3.5 ± 0.8
IRS10EE	8.92	4.62	-121.0 ± 1.8	-122.2 ± 0.7	-121.6 ± 1.9	3738	M1III	-113.0 ± 1.1
7.69-6.48	7.69	-6.48	...	-28.0 ± 1.0	-28.0 ± 1.0	4329	K2III	...
ID94	-3.87	-9.61	-11.1 ± 1.8	-8.5 ± 1.0	-9.8 ± 2.1	4144	K3III	-7.5 ± 1.1
G1044	-3.82	9.70	192.1 ± 1.8	189.1 ± 0.7	190.6 ± 1.9	3348	M7III	199.9 ± 0.8
-9.28+5.33	-9.28	5.33	201.8 ± 1.8	...	201.8 ± 1.8	4110	K4III	...
6.56+8.47	6.56	8.47	62.0 ± 1.8	...	62.0 ± 1.8	4469	K1III	...
-6.67-8.52	-6.67	-8.52	-74.3 ± 1.8	...	-74.3 ± 1.8	4708	G9III	...
G1130	-5.90	9.27	-28.4 ± 1.8	-22.9 ± 1.0	-25.6 ± 2.1	3679	M2III	-20.6 ± 1.1
-7.20-8.51	-7.20	-8.51	38.4 ± 1.8	...	38.4 ± 1.8	3861	M0III	...
G1061?	11.02	1.71	178.6 ± 1.8	177.7 ± 0.7	178.1 ± 1.9	3324	M7III	184.8 ± 1.1
ID460	-8.44	7.31	-107.7 ± 1.8	...	-107.7 ± 1.8	3916	K5III	-100.0 ± 1.1
-4.87+10.0	-4.87	10.06	-56.9 ± 1.8	...	-56.9 ± 1.8	4608	K0III	...
ID410	9.94	5.21	-110.4 ± 1.8	...	-110.4 ± 1.8	4611	K0III	-107.0 ± 1.1
-5.33+9.93	-5.33	9.93	20.5 ± 1.8	...	20.5 ± 1.8	3828	M0III	...
G1150	-9.21	6.59	8.0 ± 1.8	...	8.0 ± 1.8	3348	M7III	15.6 ± 1.1
ID134	8.34	-7.67	...	-14.1 ± 0.7	-14.1 ± 0.7	5156	<G8III	-9.3 ± 1.1
4.36-10.47	4.36	-10.47	...	-108.6 ± 1.0	-108.6 ± 1.0	4527	K0III	...
ID366	-11.06	2.93	-38.7 ± 1.8	...	-38.7 ± 1.8	4207	K3III	-32.9 ± 1.1
ID171	-10.03	-5.64	17.3 ± 1.8	...	17.3 ± 1.8	4067	K4III	24.5 ± 1.1
ID68	-4.88	-10.55	-68.3 ± 1.8	-68.8 ± 1.0	-68.6 ± 2.1	4230	K3III	-64.8 ± 1.1
3.49+11.12	3.49	11.12	60.6 ± 1.8	...	60.6 ± 1.8	4492	K1III	...
ID534	1.96	11.52	-244.6 ± 1.8	-249.8 ± 1.0	-247.2 ± 2.1	4187	K3III	-240.0 ± 1.1
IRS15N	0.98	11.76	-18.0 ± 1.8	-21.3 ± 0.7	-19.6 ± 1.9	3579	M3III	-11.2 ± 0.8
G1152	-3.26	11.36	-51.2 ± 1.8	-52.4 ± 0.7	-51.8 ± 1.9	3648	M2III	-43.5 ± 1.1
G1174?	9.63	7.11	-4.9 ± 1.8	-5.7 ± 0.7	-5.3 ± 1.9	4112	K3III	-0.1 ± 1.1
G1124?	12.01	-0.09	223.8 ± 1.8	221.3 ± 0.7	222.5 ± 1.9	4476	K1III	224.8 ± 1.1
G1183	-0.88	12.00	-11.6 ± 1.8	-14.5 ± 0.7	-13.1 ± 1.9	3578	M3III	-4.6 ± 1.1
6.33-10.28	6.33	-10.28	115.8 ± 1.8	...	115.8 ± 1.8	4363	K1III	...
G1118?	8.34	8.74	48.4 ± 1.8	51.5 ± 1.0	50.0 ± 2.1	4151	K3III	47.9 ± 1.1
8.25-8.93	8.25	-8.93	...	-175.4 ± 1.0	-175.4 ± 1.0	5857	<G8III	...
ID404	-11.14	4.98	-85.4 ± 1.8	...	-85.4 ± 1.8	3900	K5III	-77.1 ± 1.1

Table 3—Continued

Name	RA (″)	DEC (″)	V99 (km s^{-1})	V05 (km s^{-1})	V$_{avg}$ (km s^{-1})	Temp (K)	Spectral Type	V$_{Figer}$ (km s^{-1})
G1198	-4.95	11.17	-141.4 ± 1.8	-142.4 ± 1.0	-141.9 ± 2.1	3709	M1III	-133.0 ± 1.1
ID491	-8.08	9.20	38.0 ± 1.8	...	38.0 ± 1.8	4388	K1III	38.2 ± 1.1
G1248	6.59	-10.34	76.9 ± 1.8	82.9 ± 1.0	79.9 ± 2.1	4106	K4III	80.6 ± 1.1
4.29+11.49	4.29	11.49	243.6 ± 1.8	239.8 ± 0.7	241.7 ± 1.9	4579	K0III	...
G1266	-9.43	7.90	-121.0 ± 1.8	...	-121.0 ± 1.8	4502	K0III	-113.0 ± 1.1
ID261	12.45	-1.67	156.6 ± 1.8	153.2 ± 1.0	154.9 ± 2.1	4199	K3III	158.8 ± 1.1
IRS28	11.41	-5.63	-54.4 ± 1.8	-62.7 ± 0.7	-58.6 ± 1.9	3387	M6III	-47.6 ± 1.1
12.78-0.38	12.78	-0.38	...	54.5 ± 0.7	54.5 ± 0.7	3764	M1III	...
G1187?	7.05	10.71	62.5 ± 1.3	62.7 ± 0.7	62.6 ± 1.5	3568	M3III	71.0 ± 0.8
G1202?	12.16	4.38	73.1 ± 1.8	72.7 ± 0.7	72.9 ± 1.9	3414	M6III	79.9 ± 1.1
12.76+2.06	12.76	2.06	...	175.6 ± 1.0	175.6 ± 1.0	3261	>M7III	...
9.33+9.04	9.33	9.04	-34.6 ± 1.8	...	-34.6 ± 1.8	4566	K0III	...
G1306	-6.71	11.28	5.1 ± 1.8	...	5.1 ± 1.8	4037	K4III	11.2 ± 1.1
-8.83-10.2	-8.83	-10.20	80.1 ± 1.8	...	80.1 ± 1.8	4280	K2III	...
G1311	5.71	12.23	81.1 ± 1.8	78.9 ± 0.7	80.0 ± 1.9	3682	M2III	84.5 ± 0.8
G1390?	12.25	-6.32	-225.7 ± 1.8	-228.4 ± 0.7	-227.1 ± 1.9	3798	M0III	-218.0 ± 1.1
13.28-3.86	13.28	-3.86	...	-63.8 ± 1.0	-63.8 ± 1.0	4539	K0III	...
G1438?	-10.48	-9.18	45.8 ± 1.8	...	45.8 ± 1.8	3522	M4III	53.9 ± 1.1
ID506	-9.74	10.02	-34.0 ± 1.8	...	-34.0 ± 1.8	4326	K2III	-27.7 ± 1.1
G1271?	12.35	6.59	-56.5 ± 1.8	-51.9 ± 0.7	-54.2 ± 1.9	4083	K4III	-53.3 ± 1.1
G1458	-10.87	9.04	28.3 ± 1.8	...	28.3 ± 1.8	3504	M4III	36.8 ± 1.1
13.16-5.31	13.16	-5.31	...	-64.7 ± 1.0	-64.7 ± 1.0	2948	>M7III	...
G1334?	12.28	7.66	-151.8 ± 1.8	-143.8 ± 0.7	-147.8 ± 1.9	4323	K2III	-144.0 ± 1.1
13.01+6.47	13.01	6.47	...	60.2 ± 1.0	60.2 ± 1.0	3485	M4III	...
ID109	12.39	-8.80	-25.5 ± 1.8	-24.8 ± 0.7	-25.1 ± 1.9	3531	M4III	-17.9 ± 1.1
IRS11SW	-10.21	11.65	-97.2 ± 1.8	...	-97.2 ± 1.8	3575	M3III	-91.6 ± 1.1
-11.45-10.	-11.45	-10.91	-12.5 ± 1.8	...	-12.5 ± 1.8	4335	K2III	...
ID575	8.22	13.81	...	135.0 ± 1.0	135.0 ± 1.0	4819	G8III	143.3 ± 1.1
9.96+13.12	9.96	13.12	...	35.4 ± 1.0	35.4 ± 1.0	4547	K0III	...
ID566	11.18	13.51	...	36.9 ± 1.0	36.9 ± 1.0	4380	K1III	44.1 ± 1.1
ID580	11.79	13.85	...	180.7 ± 1.0	180.7 ± 1.0	4889	G8III	182.8 ± 1.1
12.23+13.5	12.23	13.57	...	32.4 ± 1.0	32.4 ± 1.0	4691	G9III	...
12.63+14.1	12.63	14.10	...	49.2 ± 1.0	49.2 ± 1.0	4449	K1III	...

Note. — Radial velocity of individual cool stars derived from the Dopplor shift of the CO (2-1) band head feature. Designations of the stars are taken from Figer et al. (2003) and Tanner et al. (2006). For those objects which were not included in the previous works, we use their coordinates as the designation. Velocity measurements in two epochs 1999 and 2005 are listed when available. The temperatures and spectral types are calculated with measured average equivalent widths of the CO feature using the method describe in Tanner et al. (2006). Values in the last two columns are taken from Figer et al. (2003), which was based on the same two data sets obtained in 1999.

Table 4.   Cool Star Velocity Statistics

GC	1	2	3	4	1 ∪ 2	1 ∩ 2	3 ∪ 4	3 ∩ 4	1 ∪ 2 ∪ 3 ∪ 4
Number of stars	98	30	68	68	102	26	86	50	123
$V_{average}$ (km s^{-1})	-9.6	-23.2	-18.0	-1.6	-9.2	-27.0	-6.6	-15.3	-4.9
V_{median} (km s^{-1})	-5.7	11.6	-20.1	-7.4	-5.7	11.0	-10.7	-14.5	-7.8
V_{stddev} (km s^{-1})	111.6	107.8	110.8	130.3	111.3	108.4	122.3	119.1	113.7
$V_{skewness}$ (km s^{-1})	-0.2	-1.3	-0.2	-0.1	-0.2	-1.3	0.0	-0.4	0.0
$V_{kurtosis}$ (km s^{-1})	0.5	1.4	0.7	0.6	0.5	1.5	0.7	0.6	0.8
(V2-V1)$_{average}$ (km s^{-1})						3.1		3.6	
(V2-V1)$_{stddev}$ (km s^{-1})						2.5		1.5	
Gaussian V_{Center} (km s^{-1})	1.1	31.7	-2.2	11.7	4.7	27.2	3.7	4.5	4.2
Gaussian σ_V (km s^{-1})	81.9	69.2	78.1	86.1	86.1	62.8	88.2	74.1	89.2

Note. — Statistical results based on the velocity distribution of cool star samples.

Table 5.   Radial Velocities of Narrow He I Line Stars

Name	RA arcsec	Dec arcsec	V1 km s^{-1}	V2 km s^{-1}	V3 km s^{-1}	V4 km s^{-1}	V$_{avg}$ km s^{-1}	ΔV km s^{-1}	EW Å	Ref.
IRS16NW	0.22	1.04	-55.6± 13.9	-55.4± 7.9	-63.9± 11.7	-64.1± 16.2	-59.7± 6.4	-11.9± 3.0	1.87	(1),(2),(3),(6)
IRS16C	1.32	0.45	113.5± 13.4	89.4± 2.6	104.3± 15.7	102.1± 16.6	102.3± 6.7	-8.9± 3.0	1.53	(1),(2),(3),(6)
IRS16SW(W)	1.43	-1.22	465.5± 16.9	433.6± 2.4	424.8± 2.8	380.4± 3.3	426.1± 4.4	-53.3± 13.5	1.47	(1),(2),(3),(4),(6)
IRS16CC	2.26	0.52	248.3± 6.1	241.1± 3.0	241.5± 4.2	255.1± 4.0	246.5± 2.2	1.6± 3.0	1.68	(1),(3),(4),(6)
IRS33N	0.30	-2.49	...	-135.1± 14.5	39.5± 3.2	37.8± 0.3	-19.2± 5.0	-8.6± 6.0	2.43	(3),(5),(6)
MPE+1.0-7.4	1.66	-2.03	...	82.9± 9.3	...	...	82.9± 9.3	...	2.75	(6)
MPE-2.0-8.5	-1.30	-3.11	-131.9± 3.6	...	...	-125.7± 2.5	-128.8± 2.2	37.8± 3.0	2.05	
IRS16NE	3.24	1.08	12.8± 18.6	-2.4± 12.2	-35.6± 23.7	-63.4± 2.7	-22.2± 8.2	-45.6± 3.0	1.11	(1),(2),(3),(6)
IRS33E	1.12	-3.41	148.0± 15.5	129.0± 14.1	125.2± 2.6	111.1± 2.6	128.3± 5.3	-16.1± 10.5	1.46	(1),(2),(3),(6)
IRS34W	-4.11	1.23	-316.2± 1.6	...	-289.9± 3.2	...	-303.1± 1.8	24.7± 3.0	1.11	(1),(2),(6)
IRS7SE	2.41	4.58	-128.1± 4.2	...	-122.5± 4.6	-116.2± 2.6	-122.3± 2.2	8.2± 6.0	1.87	(1),(6)
A21	5.28	-3.51	-185.7± 2.7	-232.4± 22.7	-174.5± 3.9	-179.5± 1.9	-193.0± 5.8	7.6± 4.5	1.77	
ID308^a	6.67	0.55	-3.9± 5.8	-24.8± 2.7	-44.0± 5.5	-19.1± 5.6	-22.9± 2.5	-7.6± 3.0	1.52	(6)
MPE+1.41-12.2	2.46	-6.69	121.4± 16.2	97.6± 21.3	96.3± 6.0	97.1± 11.8	103.1± 7.5	-6.8± 3.0	2.66	(6)
IRS26	-1.37	7.80	-109.2± 10.6	-124.0± 2.2	-118.0± 20.3	-111.2± 14.8	-115.6± 6.8	-16.9± 3.0	1.75	(6)
IRS6W	-7.91	0.82	62.9± 3.0	...	...	...	62.9± 3.0	...	1.52	(1),(3)
A12	-0.20	8.72	-127.4± 16.3	-151.2± 1.1	...	-166.7± 3.3	-148.4± 5.6	-2.9± 3.0	1.91	(3),(6)
AFNWB	-8.08	-3.92	224.3± 17.0	...	...	...	224.3± 17.0	...	2.02	(3)
G1138	-8.12	-7.02	154.4± 5.5	...	...	...	154.4± 5.5	...	4.12	(3)
-8.91-6.76	-8.91	-6.76	85.3± 5.9	...	...	...	85.3± 5.9	...	1.90	(3)

Note. — Radial velocity measurements of narrow type He I stars from four data sets. The eqivarlent width for each object is calculated from the average width of the fitted Gaussian componets.

^{a}Source name is taken from Figer et al. (2003)

^{b}Source name is taken from Ott et al. (2003)

References.   — (1) Genzel et al. (2000); (2) Paumard et al. (2001); (3) Tanner et al. (2006); (4) Paumard et al. (2003); (5) Paumard et al. (2004); (6) Paumard et al. (2006).

Table 6. Radial Velocities of Broad He I Line Stars

Name	RA arcsec	Dec arcsec	V1 km s^{-1}	V2 km s^{-1}	V3 km s^{-1}	V4 km s^{-1}	V$_{avg}$ km s^{-1}	ΔV km s^{-1}	EW Å	Ref.
IRS13E	-2.82	-2.09	143.4± 61.4	168.9± 37.3	164.8± 60.1	144.6± 73.0	155.4± 29.7	8.2± 3.0	23.33	(2),(6)
IRS7W	-4.14	4.67	-193.9± 27.1	-199.1± 24.1	-163.7± 59.1	...	-185.6± 23.1	0.0± 3.0	203.05	(1),(2),(3),(6)
GCHe2	3.64	-5.86	253.1± 100.8	479.8± 144.6	305.4± 51.7	253.4± 40.2	322.9± 47.0	-54.1± 27.0	265.75	(2),(3),(6)
ID415[a]	4.62	5.42	-23.2± 8.1	...	-48.5± 21.8	-53.9± 23.3	-41.9± 11.0	-10.0± 3.0	71.56	(1),(2),(4),(6)
AFNW	-7.53	-4.34	187.9± 39.7	...	...	...	187.9± 39.7	...	228.30	(1),(2),(3),(6)
ID180[b]	9.74	0.80	...	...	-16.4± 120.2	...	-16.4± 120.2	...	77.04	(2),(6)
AF	-6.14	-7.81	243.7± 17.4	...	...	...	243.7± 17.4	...	290.19	(1),(2),(3),(6)
IRS15SW	-1.77	10.08	-119.6± 24.2	...	-62.1± 105.0	-124.8± 32.4	-102.2± 37.5	10.3± 3.0	270.48	(1),(2),(3),(6)
IRS9S	6.45	-8.32	347.2± 33.7	54.9± 267.5	325.9± 18.0	324.5± 5.9	263.1± 67.6	0.0± 3.0	41.31	(1),(3),(6)

Note. — Radial velocity measurements of broad type He I stars from four data sets. The eqivarlent width for each object is calculated by integrating the area below the normalized spectrum within the ±1000 km s^{-1} wavelength range of the corresponding spectral line emission peak.

[a]Source name is taken from Figer et al. (2003)

[b]Source name is taken from Ott et al. (2003)

References. — (1) Genzel et al. (2000); (2) Paumard et al. (2001); (3) Tanner et al. (2006); (4) Paumard et al. (2003); (5) Paumard et al. (2004).

Table 7.   Spectral Types of He I Line Stars

Name	RA arcsec	Dec arcsec	P2006[a] Designation	Alternative Name	He I Line Width	Spectral[a] Type
IRS16NW	0.22	1.04	E19		Narrow	Ofpe/WN9
IRS16C	1.32	0.45	E20		Narrow	Ofpe/WN9
IRS16SW(W)	1.43	-1.22	E23	IRS16SW,	Narrow	Ofpe/WN9
IRS16CC	2.26	0.52	E27		Narrow	O9.5-B0.5 I
IRS33N	0.30	-2.49	E33	A11	Narrow	B0.5-1 I
MPE+1.0-7.4	1.66	-2.03	E34	IRS16S	Narrow	B0.5-1 I
MPE-2.0-8.5	-1.30	-3.11	E43		Narrow	O8.5-9.5 I
IRS16NE	3.24	1.08	E39		Narrow	Ofpe/WN9
IRS33E	1.12	-3.41	E41	ID221, IRS33SE	Narrow	Ofpe/WN9
IRS34W	-4.11	1.23	E56		Narrow	Ofpe/WN9
IRS7SE	2.41	4.58	E62		Narrow	B0-3 I
A21	5.28	-3.51			Narrow	
ID308	6.67	0.55	E67	IRS1E	Narrow	B1-3 I
MPE+1.41-12.2	2.46	-6.69	E69		Narrow	
IRS26	-1.37	7.80	E73		Narrow	O9-B I
IRS6W	-7.91	0.82			Narrow	
A12	-0.20	8.72	E75		Narrow	O9-B I
AFNWB	-8.08	-3.92			Narrow	
G1138	-8.12	-7.02			Narrow	
-8.91-6.76	-8.91	-6.76			Narrow	
IRS13E	-2.82	-2.09	E51(?)		Broad	WN8(?)
IRS7W	-4.14	4.67	E68(?)		Broad	WC9(?)
GCHe2	3.64	-5.86	E65	IRS9W	Broad	WN8
ID415	4.62	5.42	E70	IRS7E2	Broad	Ofpe/WN9
AFNW	-7.53	-4.34	E74	AHHNW	Broad	WN8
ID180	9.74	0.80	E78	HeI N1	Broad	WC9
AF	-6.14	-7.81	E79	AHH	Broad	Ofpe/WN9
IRS15SW	-1.77	10.08	E83		Broad	WN8/WC9
IRS9S	6.45	-8.32	E80	IRS9SE	Broad	WC9

[a]Designations and spectral types are taken from Paumard et al. (2006)